Prediction of evolving plasticity in rails under steady state rolling contact based on Reduced-Order Modeling

(article starts on next page)

Prediction of evolving plasticity in rails under steady state rolling contact based on Reduced-Order Modeling

Caroline Ansin [ID] *, Fredrik Larsson, Ragnar Larsson

Division of Material and Computational Mechanics/ CHARMEC, Chalmers University of Technology, SE-412 96, Gothenburg, Sweden

ARTICLE INFO

ABSTRACT

Predicting railhead damage due to multiple wheel passes in railway operations can be computationally demanding, especially when accounting for the rail's inelastic material response. In this paper, we use a steady-state assumption within a convective coordinate system and employ Reduced-Order Modeling (ROM) through the Proper Generalized Decomposition (PGD) method to increase the computational efficiency. Our approach solves a nonlinear reduced-order problem for the displacements in a 3D railhead with elastic–plastic material properties considering various contact scenarios. The ROM framework includes domain decomposition and a parametric loading framework using PGD. It accounts for the elastic–plastic rail material through three key features: (1) treatment of the moving load under the assumption of steady state, by using a convective coordinate system along the railhead to convert the problem into a stationary contact load problem, (2) implementation of PGD to solve the 3D displacement field efficiently, and (3) use of fixed-point iterations to treat the coupling for solving plastic strains and displacements. In this iterative process, plastic strains are solved from displacements, and displacements are solved based on a loading scenario and updated plastic strains. The accuracy and computational efficiency are assessed by comparing our strategy with 3D finite element simulations for moving contact loads. The results show convergence with only a few fixed-point iterations for each over rolling, which results in a solution that is 63 times faster. This efficiency is crucial for assessing the accumulated plastic deformation from multiple wheel passes.

1. Introduction

The contact between the wheel and the rail in railway operations results in high contact stresses, causing wear and plastic deformation to accumulate at the rail surface. Over time, with many wheel passes, this cumulative effect can lead to changes in the rail geometry, as well as the formation and propagation of cracks. Therefore, effective maintenance strategies are essential to prevent rail failure and extend the life of the rail. Additionally, minimizing service disruptions, ensuring operational safety, and reducing costs are crucial. Numerical computations offer a promising approach for predicting rail damage, which can optimize maintenance procedures.

Previous work [1–5] has proposed a methodology to compute long-term railhead surface damage. The approach involves a series of steps applied in repetition: (1) For a given traffic scenario, multibody simulations of dynamic vehicle-track interactions are computed to provide information about the position and the magnitude of the contact load. (2) The wheel-rail contact in the normal direction is analyzed to understand the elastic–plastic behavior under load. (3) Cumulative damage is evaluated by considering both plasticity and surface wear. The framework also predicts surface rolling contact fatigue. (4) Finally, the railhead profile is updated

---

* Corresponding author.

E-mail address: caroline.ansin@chalmers.se (C. Ansin).

from accumulative wear and plasticity. To accelerate the framework, the second step utilizes a metamodel to evaluate the elastic–plastic contact, and the third step limits the elastic–plastic computation to a 2D analysis, which does not fully capture the complexity of railhead behavior under contact.

To address the limitations of the two-dimensional analysis, we propose transitioning to a more comprehensive 3D description of elastic–plastic computation. This transition allows for a more accurate representation of phenomena such as contact stress distribution, Poisson's effects in the railhead, and longitudinal stress propagation due to frictional contact. However, traditional 3D Finite Element (FE) methods for solving elastic–plastic wheel-rail contact under a moving contact load are computationally demanding for each wheel pass. This method has been extensively used in works such as [6–10].

Traditional 3D Finite Element (FE) simulations are typically performed in a Lagrangian frame $x_0 = (x_0, y_0, z_0)$ as shown in Fig. 1a. These simulations require numerous time steps t to model the moving contact load t along the railhead. Also, a fine discretization near the contact area (illustrated in blue in the Figure), with a contact location that can shift depending on the contact scenario, is crucial to capture the material response accurately. This fine discretization is required for the entire length of the railhead since the contact load moves along the railhead. Moreover, achieving a stable solution and mitigating boundary effects associated with the contact load rolling over the railhead's edge requires considering a long railhead section. As a result, evaluations are limited to a specific region of interest (shown in the Figure), since including the unloaded part or accounting for boundary effects would result in inaccurate results. All of these factors extend the simulation times, whereby many over rollings are rarely considered.

(a) *Lagrangian frame*   **(b)** *Convective coordinate system frame*
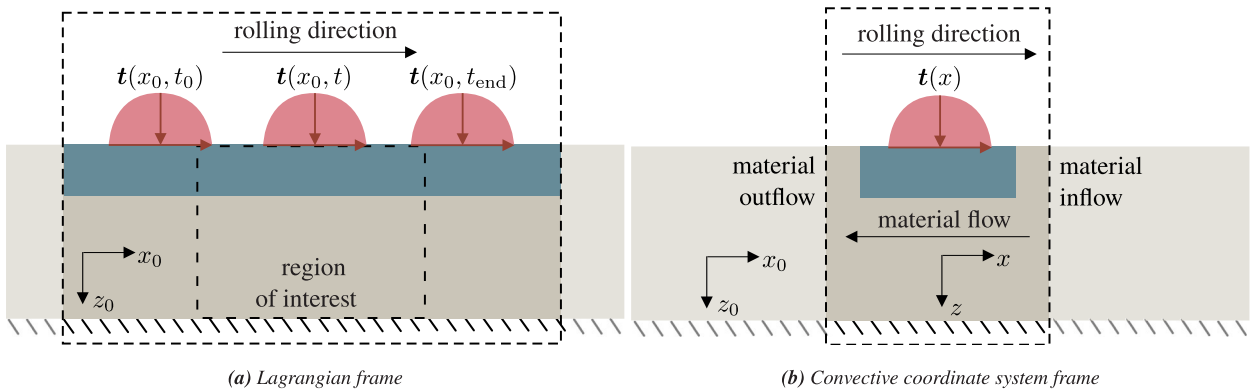
Fig. 1. Comparison of moving surface traction t in (a) the Lagrangian frame $x_0 = (x_0, y_0, z_0)$, which requires a longer railhead and multiple time steps t, and (b) the convective coordinate system $x = (x, y, z)$, which simplifies the problem to a stationary one. Material flows in from the right boundary and out from the left. The blue region illustrates where a fine discretization is necessary. (For interpretation of the references to color in this figure legend, the reader is referred to the web version of this article.)

A convective coordinate system $x = (x, y, z)$ and assuming steady state can be used to address the computational challenges with traditional 3D FE simulations, as shown in Fig. 1b. This has been demonstrated in [11–15] for rails and pavement structures under an applied contact load and in [16–22] for both bodies in rolling contact. The convective coordinate system moves with the velocity of the contact load through space. As a result, the contact load becomes stationary and the material response becomes time independent, expressed in terms of spatial variation instead. Thus, each wheel pass can be solved from a single load increment, resulting in lower computational costs. Moreover, it requires a fine mesh (illustrated in blue in the Figure) only at the contact area, and a shorter railhead section can be discretized compared to the Lagrangian approach.

Incorporating nonlinear rail material behavior in the convective coordinate system can lead to issues since the material is not fixed to the FE mesh. It can result in large computations because of the coupling between material tangents and displacements, and potential asymmetry in the stiffness matrix. This can be solved by tracking the material history at each integration point along the streamlines within the FE mesh to update the state variables, as done in previous studies [11–13,22,23]. It involves reading the material history of the prior integration point upwind. Fig. 1b shows how the material flows in at the right boundary, travels along the streamline, and flows out at the left boundary.

The computational complexity can also be reduced by implementing a Reduced-Order Model (ROM), e.g., the Proper Generalized Decomposition (PGD) method [24–26]. This method is useful for applications such as parametric modeling [27–33] and high-dimensional problems [24,25,34,35]. In our previous work [36], we used PGD to efficiently solve the displacement field. There, we demonstrated the ability to accurately predict the elastic response of the railhead in various contact load scenarios using PGD. Specifically, the PGD model includes a domain decomposition of the 3D solid railhead considering a two-dimensional in-plane cross-section $y = (y, z)$ and a one-dimensional out-of-plane discretization x as parameters in the PGD approximation. This domain decomposition, as proposed by [30,37,38], allows the the fully 3D displacement field $u(y, x)$ to be approximated as a finite sum of unknown functions Y_n (vectorial, 3D) and X_n (scalar), respectively, as

$$u(y, x) \approx \sum_{n=1}^{N} Y_n(y) \, X_n(x), \tag{1}$$

enriching the solution iteratively. Furthermore, the distributed contact load can be parameterized and incorporated as additional coordinates in the PGD formulation. The load, predicted from dynamic vehicle-track simulations, is described using a semi-Hertzian contact [39,40]. By incorporating this approach, numerous contact scenarios can be accommodated effectively while maintaining computational efficiency comparable to that of two-dimensional methods.

In this work, we propose a ROM framework to efficiently address the evolving plasticity in a railhead by expanding on the PGD model developed in [36]. This approach incorporates three key components: (1) assuming a steady state of the moving contact load within the convective coordinate system to simplify the problem to a stationary contact problem, (2) implementing an iterative scheme to manage the coupling between the displacement field and plastic strain, and (3) using the PGD method with a domain decomposition outlined in [36] to solve the displacement field efficiently. Moreover, parallel processing for plastic strain computations speeds up the computation by treating each integration point in the cross-section independently.

The present study examines different Hertzian contact pressures [41] for our proposed ROM. Our results for one and multiple over rollings are validated against results from a moving contact load analysis solved using 3D finite elements in commercial software. In addition, the evolving plasticity of the railhead is investigated given a load collective.

2. Problem description - 3D elastic–plastic solid railhead analysis

We shall analyze the straight 3D solid railhead section shown in Fig. 2. The railhead material is modeled as elastic–plastic, with a focus on studying the effects of evolving plasticity for a moving contact load. The load is represented as a distributed surface pressure that moves with the velocity $\bar{v}$. The analysis assumes a small deformation framework. We want to evaluate state variables, such as plastic strains ϵ^{p}, and the displacement field u within the railhead. The simulations will consider steady-state conditions of moving contact loads and deal with the coupling to solve the displacement field and plastic strain with an iterative scheme, which will be elaborated on in later sections. The PGD method is used to compute the displacement field efficiently. The study will consider both single over rolling events and multiple passes over the rail.
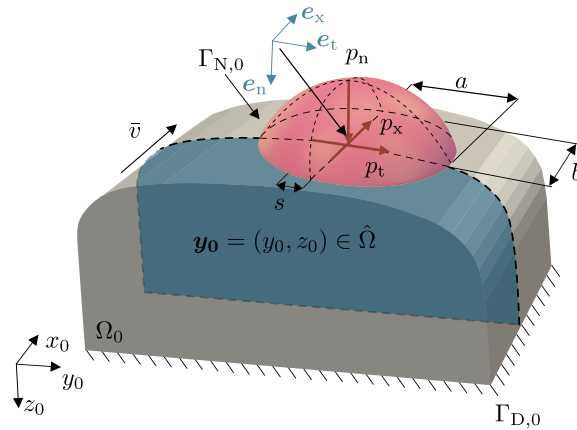
Fig. 2. A 3D railhead section Ω_0 with a Hertzian [41] surface pressure $q = (s, a, b, p_{\mathrm{n}}, p_{\mathrm{t}}, p_{\mathrm{x}})$ moving along $\Gamma_{\mathrm{N},0}$, positioned at s with semi-axes a and b. The maximum tractions p_{n}, p_{t}, and p_{x} act in the directions e_{n}, e_{t}, and e_{x}, defined locally from the contact center. The displacements are fixed at $\Gamma_{\mathrm{D},0}$. The cross-section coordinates are $y_0 = (y_0, z_0) \in \hat{\Omega}$, while $x_0 \in (-\infty, \infty)$ is the out-of-plane coordinate.

2.1. Momentum balance

To describe the mechanical response of the infinitely long railhead within the domain Ω_0 shown in Fig. 2, we consider the balance of linear momentum under the assumption of quasi-static loading conditions. Neglecting body forces, the governing equation reads

$$-\sigma \cdot \nabla_0 = 0 \quad \text{in} \quad \Omega_0 := \hat{\Omega} \times (-\infty, \infty), \tag{2a}$$

$$u = 0 \quad \text{on} \quad \Gamma_{\mathrm{D},0} := \hat{\Gamma}_{\mathrm{D}} \times (-\infty, \infty), \tag{2b}$$

$$\sigma \cdot n = t(q; y_0, x_0 - \bar{v}t) \quad \text{on} \quad \Gamma_{\mathrm{N},0} := \hat{\Gamma}_{\mathrm{N}} \times (-\infty, \infty). \tag{2c}$$

Here, σ denotes the Cauchy stress tensor and n is the outward normal to the surface. The del operator ∇_0, related to the fixed coordinate system $x_0 = (x_0, y_0, z_0)$, is defined as $\nabla_0 = \partial e_x / \partial x_0 + \partial e_y / \partial y_0 + \partial e_z / \partial z_0$ with e_x, e_y and e_z being the local unit base vectors aligned with the railhead profile in the center of the contact load (see Fig. 2). Displacements are fixed at the bottom of the railhead $\Gamma_{\mathrm{D},0}$, while distributed surface traction t is applied on the surface $\Gamma_{\mathrm{N},0}$. The traction is assumed stationary, centered around $x_0 = \bar{v}t$ with the velocity $\bar{v} = \bar{v}e_x$, and is parametric by some load scenario q, e.g., a Hertzian pressure distribution [41]. The cross-section of the railhead reads $y_0 = (y_0, z_0) \in \hat{\Omega}$ and the out-of-plane coordinate $x_0 \in (-\infty, \infty)$.

2.2. Constitutive relations of elasto-plasticity

To capture ratcheting in rail material under multiple over rollings, we use the Ohno–Wang model [42], which incorporates linear isotropic elasticity and nonlinear kinematic hardening. An overview of the constitutive model is provided in this Section, for a detailed description, refer to [43].

In the small deformation framework, we consider the constitutive relations of isotropic plasticity as

$$\boldsymbol{\sigma} = \mathbf{E} : \boldsymbol{\epsilon}^{\mathrm{e}}, \quad \boldsymbol{\epsilon}^{\mathrm{e}} = \boldsymbol{\epsilon} - \boldsymbol{\epsilon}^{\mathrm{p}}, \tag{3}$$

with the strain tensor $\boldsymbol{\epsilon}$ being related to the displacement $\boldsymbol{u}$ as $\boldsymbol{\epsilon}[\boldsymbol{u}] = 1/2\,([\nabla_0 \otimes \boldsymbol{u}] + [\nabla_0 \otimes \boldsymbol{u}]^{\mathrm{T}})$ and can be separated into its elastic component $\boldsymbol{\epsilon}^{\mathrm{e}}$ and plastic component $\boldsymbol{\epsilon}^{\mathrm{p}}$. The 4th order constant elasticity tensor is defined as $\mathbf{E} = 2G\mathbf{I} + K_{\mathrm{b}}\boldsymbol{I} \otimes \boldsymbol{I}$, where $\mathbf{I}$ and $\boldsymbol{I}$ are the 4th and 2nd order identity tensors, respectively, and G and K_{b} are the shear and bulk modulus, respectively.

The von Mises yield function Φ is adopted and can be expressed as

$$\Phi = \sigma_{\mathrm{e}}^{\mathrm{red}} - \sigma_{\mathrm{y}}, \quad \sigma_{\mathrm{e}}^{\mathrm{red}} := \sqrt{\frac{3}{2}}|\boldsymbol{\sigma}^{\mathrm{red}}|, \quad \boldsymbol{\sigma}^{\mathrm{red}} = \boldsymbol{\sigma}_{\mathrm{dev}} - \boldsymbol{\alpha}, \tag{4}$$

where the stress tensor $\boldsymbol{\sigma}$ is divided into its volumetric $\boldsymbol{\sigma}_{\mathrm{vol}} = \boldsymbol{I} : \boldsymbol{\sigma}$ and deviatoric part $\boldsymbol{\sigma}_{\mathrm{dev}} = \boldsymbol{\sigma} - \boldsymbol{\sigma}_{\mathrm{vol}}/3\boldsymbol{I}$. Furthermore, $\sigma_{\mathrm{e}}^{\mathrm{red}}$ is the effective (reduced) stress, σ_{y} is the yield limit, and $\boldsymbol{\alpha} = \sum_{i=1}^{n_{\mathrm{b}}} \boldsymbol{\alpha}^i$ is the sum of all n_{b} back-stresses due to kinematic hardening.

The plastic flow rule and the kinematic hardening evolution rule governing the plastic strain $\dot{\boldsymbol{\epsilon}}^{\mathrm{p}}$ and back stresses $\dot{\boldsymbol{\alpha}}^i$ for $i = (1, \ldots, n_{\mathrm{b}})$ are given by

$$\dot{\boldsymbol{\epsilon}}^{\mathrm{p}} = \lambda \boldsymbol{\nu}, \quad \boldsymbol{\nu} = \frac{\partial \Phi}{\partial \boldsymbol{\sigma}} = \frac{3}{2\sigma_{\mathrm{e}}^{\mathrm{red}}} \boldsymbol{\sigma}_{\mathrm{dev}}, \quad \boldsymbol{\epsilon}^{\mathrm{p}}(\boldsymbol{y}_0, x_0, 0) = \boldsymbol{\epsilon}_0^{\mathrm{p}}(\boldsymbol{y}_0, x_0), \tag{5a}$$

$$\dot{\boldsymbol{\alpha}}^i = \frac{2}{3} C_i \dot{\boldsymbol{\epsilon}}^{\mathrm{p}} - \frac{\gamma_i^{m_i+1}}{C_i^{m_i}} \alpha_{\mathrm{e}}^{i,m_i} < \dot{\boldsymbol{\epsilon}}^{\mathrm{p}} : \boldsymbol{\alpha}^i > \frac{\boldsymbol{\alpha}^i}{\alpha_{\mathrm{e}}^i}, \quad \alpha_{\mathrm{e}}^i := \sqrt{\frac{3}{2}}|\boldsymbol{\alpha}^i|, \quad \boldsymbol{\alpha}^i(\boldsymbol{y}_0, x_0, 0) = \boldsymbol{\alpha}_0^i(\boldsymbol{y}_0, x_0), \tag{5b}$$

where C_i, γ_i and m_i are material parameters, and $\boldsymbol{\epsilon}_0^{\mathrm{p}}(\boldsymbol{y}_0, x_0)$ and $\boldsymbol{\alpha}_0^i(\boldsymbol{y}_0, x_0)$ are initial conditions defined at time $t = 0$. The plastic multiplier λ is determined from the Kuhn–Tucker loading/unloading conditions

$$\Phi(\boldsymbol{\sigma}, \boldsymbol{\alpha}) \le 0, \quad \lambda \ge 0, \quad \lambda\,\Phi(\boldsymbol{\sigma}, \boldsymbol{\alpha}) = 0. \tag{6}$$

3. Steady state for moving contact loads - 3D elastic–plastic analysis

Handling moving loads in a fixed coordinate system for 3D FE elastic–plastic analyzes is computationally demanding, since it requires many time increments. Using a convective coordinate system that moves with the load, the contact load is regarded as fixed in space with rail material in motion, as shown in Fig. 3. Furthermore, considering the steady-state solution, the deformations, stresses, and strains are independent of time. In particular, this allows for spatial integration of the evolution rules without consideration of time increments, reducing computational costs.

3.1. Kinematics

A convective coordinate system $\boldsymbol{x} = (x, y, z)$ is introduced to describe the material points in the region Ω in Fig. 3. Upon assuming steady-state conditions in this frame, it is defined by

$$\boldsymbol{x} = \boldsymbol{x}_0 - \bar{\boldsymbol{v}}t, \tag{7}$$

where $\bar{\boldsymbol{v}} = \bar{v}e_{\mathrm{x}}$ is the constant material velocity. Thus, the coordinate $x(x_0, t) = x_0 - \bar{v}t$ is time dependent, while the coordinates $y = y_0$ and $z = z_0$ remain constant. The origin of the coordinate system is placed in the center of the load as seen in Fig. 3.

For any field quantity $\boldsymbol{f}(\boldsymbol{x}, t)$ linked to the material, the spatial derivative transformation from $\boldsymbol{x}_0$ to $\boldsymbol{x}$ reads

$$\frac{\partial \boldsymbol{f}}{\partial \boldsymbol{x}_0}\bigg|_t = \frac{\partial \boldsymbol{f}}{\partial \boldsymbol{x}}\bigg|_t \cdot \frac{\partial \boldsymbol{x}}{\partial \boldsymbol{x}_0}\bigg|_t = \frac{\partial \boldsymbol{f}}{\partial \boldsymbol{x}}, \tag{8}$$

where the identity $\partial \boldsymbol{x}/\partial \boldsymbol{x}_0 = \boldsymbol{I}$ was used. Similarly, the time material derivative is

$$\dot{\boldsymbol{f}} = \frac{\partial \boldsymbol{f}}{\partial t}\bigg|_{\boldsymbol{x}_0} = \frac{\partial \boldsymbol{f}}{\partial t}\bigg|_{\boldsymbol{x}} + \frac{\partial \boldsymbol{f}}{\partial \boldsymbol{x}}\bigg|_t \cdot \frac{\partial \boldsymbol{x}}{\partial t}\bigg|_{\boldsymbol{x}_0}. \tag{9}$$

This expression can be simplified by considering the steady-state assumption, which implies that the time dependence of $\boldsymbol{f}$ vanishes, i.e., $\partial \boldsymbol{f}/\partial t|_{\boldsymbol{x}} = \boldsymbol{0}$. Additionally, using the transformation in (7), $\partial \boldsymbol{x}/\partial t|_{\boldsymbol{x}_0} = -\bar{v}e_{\mathrm{x}}$. Substituting these simplifications into (9) we obtain:

$$\dot{\boldsymbol{f}} = -\bar{v}\,e_{\mathrm{x}} \cdot \frac{\partial \boldsymbol{f}}{\partial \boldsymbol{x}} = -\bar{v}\,\frac{\partial \boldsymbol{f}}{\partial x}. \tag{10}$$

Thus, the time derivative in the Lagrangian frame is replaced by a spatial derivative in the convective coordinate system scaled by the negative velocity.
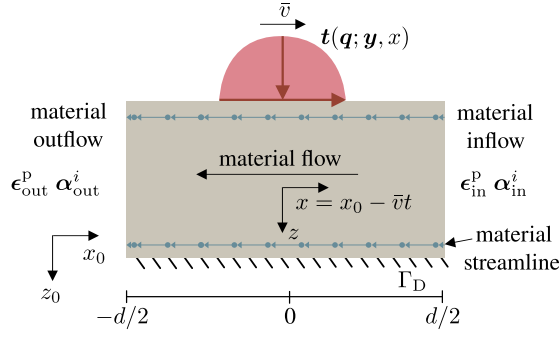
Fig. 3. Convective coordinate system $x = (x, y, z)$ moving with the contact load at constant speed $\bar{v} = \bar{v} e_x$. The boundaries of the interval $I_x = [-d/2, d/2]$ define the inflow and outflow of the state variables: $\epsilon^p_{in}(y)$, $\alpha^i_{in}(y)$, $\epsilon^p_{out}(y)$ and $\alpha^i_{out}(y)$.

3.2. Momentum balance

The momentum balance (2) is adapted to the convective coordinate system x, and will read

$$-\boldsymbol{\sigma} \cdot \boldsymbol{\nabla} = \mathbf{0} \quad \text{in} \quad \Omega := \hat{\Omega} \times I_x, \tag{11a}$$

$$\boldsymbol{u} = \mathbf{0} \quad \text{on} \quad \Gamma_D := \hat{\Gamma}_D \times I_x, \tag{11b}$$

$$\boldsymbol{\sigma} \cdot \boldsymbol{n} = \boldsymbol{t}(q; \boldsymbol{y}, x) \quad \text{on} \quad \Gamma_N := \hat{\Gamma}_N \times I_x. \tag{11c}$$

The transformation in (7) is used and the del operator $\boldsymbol{\nabla} = (\partial e_x/\partial x + \partial e_y/\partial y + \partial e_z/\partial z)$ is defined based on the relation (8). Furthermore, the interval $I_x = [-d/2, d/2]$ related to the x-variable is introduced in Fig. 3. The length parameter d represents the domain of influence to justify the far-field approximation that the boundaries $x = \pm d/2$ in the normal direction $\boldsymbol{n} = \pm e_x$ are stress-free, i.e.,

$$\boldsymbol{\sigma}(\boldsymbol{y}, \pm d/2) \cdot e_x = \mathbf{0}. \tag{12}$$

The weak form of (11) is derived by multiplying (11) with an arbitrary test function $\delta \boldsymbol{u}$, integrating over the region Ω, and using the small strain constitutive relation (3). The resulting problem reads as follows: Find the displacement field $\boldsymbol{u} \in \mathbb{U}$ such that

$$a(\boldsymbol{u}, \delta \boldsymbol{u}) - b(\epsilon^p, \delta \boldsymbol{u}) = l(q; \delta \boldsymbol{u}) \quad \forall \delta \boldsymbol{u} \in \mathbb{U}, \tag{13}$$

where

$$a(\boldsymbol{u}, \delta \boldsymbol{u}) = \int_\Omega \epsilon[\delta \boldsymbol{u}] : \mathbf{E} : \epsilon[\boldsymbol{u}] \ d\Omega, \tag{14a}$$

$$b(\epsilon^p, \delta \boldsymbol{u}) = \int_\Omega \epsilon[\delta \boldsymbol{u}] : \mathbf{E} : \epsilon^p \ d\Omega, \tag{14b}$$

$$l(q; \delta \boldsymbol{u}) = \int_{\Gamma_N} \boldsymbol{t}(q; \boldsymbol{y}, x) \cdot \delta \boldsymbol{u} \ d\Gamma. \tag{14c}$$

Here, the trial function space is defined as $\mathbb{U} := \{ \boldsymbol{v} \in [\mathbb{H}^1(\Omega)]^3 : \boldsymbol{v} = \mathbf{0} \text{ on } \Gamma_D \}$, where $\mathbb{H}^1(\Omega)$ is the space of functions on Ω with square-integrable derivatives of order zero and one.

3.3. Stationary convected formulation of plasticity

Steady-state conditions are assumed as outlined in (10) to handle the material-time derivatives of the evolution rules in (5). Thereby, the material-time derivatives are transformed into spatial derivatives along the x-axis as

$$\dot{\epsilon}^p = \frac{\partial \epsilon^p}{\partial t}\bigg|_{x_0} = -\bar{v} \frac{\partial \epsilon^p}{\partial x}, \quad \dot{\alpha}^i = \frac{\partial \alpha^i}{\partial t}\bigg|_{x_0} = -\bar{v} \frac{\partial \alpha^i}{\partial x}, \tag{15}$$

Hence, we obtain the constitutive relations as

$$-\bar{v} \frac{\partial \epsilon^p}{\partial x} = \lambda \boldsymbol{v}, \quad \epsilon^p(\boldsymbol{y}, d/2) = \epsilon^p_{in}(\boldsymbol{y}), \tag{16a}$$

$$-\bar{v} \frac{\partial \alpha^i}{\partial x} = \frac{2}{3} C_i \lambda \boldsymbol{v} - \frac{\gamma_i^{m_i+1}}{C_i^{m_i}} \alpha_e^{i,m_i} < \lambda : \alpha^i > \frac{\alpha^i}{\alpha_e^i}, \quad \alpha^i(\boldsymbol{y}, d/2) = \alpha^i_{in}(\boldsymbol{y}), \tag{16b}$$

$$\Phi(\boldsymbol{\sigma}, \boldsymbol{\alpha}) \leq 0, \quad \lambda \geq 0, \quad \lambda \, \Phi(\boldsymbol{\sigma}, \boldsymbol{\alpha}) = 0. \tag{16c}$$

Here, $\epsilon_{\text{in}}^{\text{p}}(\boldsymbol{y})$ and $\boldsymbol{\alpha}_{\text{in}}^{i}(\boldsymbol{y})$ define the initial conditions at the inflow boundary $x = d/2$ (see Fig. 3). As the material particles travel from the inflow to the outflow boundary along the material streamlines, the state variables are updated according to (16). We now consider the case of multiple load passages. Upon reaching the outflow boundary $x = -d/2$, the plastic strain and back stress have evolved as

$$^{l}\epsilon_{\text{out}}^{\text{p}}(\boldsymbol{y}) = \epsilon^{\text{p}}(\boldsymbol{y}, -d/2), \quad ^{l}\boldsymbol{\alpha}_{\text{out}}^{i}(\boldsymbol{y}) = \boldsymbol{\alpha}^{i}(\boldsymbol{y}, -d/2), \tag{17}$$

where l denotes each over rolling event, with the contact load parameters denoted as $\boldsymbol{q} = {}^{l}\boldsymbol{q}$.

To simulate multiple over rolling, the outflow values serve as the initial conditions for the next loading cycle. This ensures that the residual effects of the previous over rolling persist, such that $\epsilon_{\text{in}}^{\text{p}} = {}^{l-1}\epsilon_{\text{out}}^{\text{p}}$ and $\boldsymbol{\alpha}_{\text{in}}^{i} = {}^{l-1}\boldsymbol{\alpha}_{\text{out}}^{i}$. For the first over rolling ($l = 1$), the plastic strain and back-stress are initialized to zero: $\epsilon_{\text{in}}^{\text{p}} = \boldsymbol{0}$ and $\boldsymbol{\alpha}_{\text{in}}^{i} = \boldsymbol{0}$.

4. Reduced-order model

This section presents a ROM framework designed to solve the 3D displacement field for evolving plasticity efficiently. The framework focuses on separating displacements into elastic and plastic contributions, allowing for independent analysis. It uses the PGD method to decompose the spatial domain to reduce the complexity of the problem. State variables are updated from previous integration points along the streamline of the FE mesh, utilizing spatial variation rather than time derivatives, which additionally facilitates parallel computation. A fixed-point algorithm is used to manage the coupling between plastic strains and displacements. These strategies improve the computational efficiency and are elaborated on in the following Sections.

4.1. Preliminaries

The linearity of the weak form in (13) allows us to decompose the total displacement field $\boldsymbol{u}$ into two contributions: the elastic displacement $\boldsymbol{u}^{\text{e}}$ and the permanent deformation $\boldsymbol{u}^{\text{p}}$. This separation is expressed as

$$\boldsymbol{u} = \boldsymbol{u}^{\text{e}}[\boldsymbol{q}] + \boldsymbol{u}^{\text{p}}[\epsilon^{\text{p}}]. \tag{18}$$

Here, $\boldsymbol{u}^{\text{e}}[\boldsymbol{q}] = \boldsymbol{u}^{\text{e}} \in \mathbb{U}$ represents the displacement field under a given loading scenario $\boldsymbol{q}$ while $\boldsymbol{u}^{\text{p}}[\epsilon^{\text{p}}] = \boldsymbol{u}^{\text{p}} \in \mathbb{U}$ characterizes the displacement field arising from plastic strains ϵ^{p}. By decoupling these contributions, each component can be solved independently, leading to two equations of (13) as

$$a(\boldsymbol{u}^{\text{e}}, \delta\boldsymbol{u}) = l(\boldsymbol{q}; \delta\boldsymbol{u}) \quad \forall\delta\boldsymbol{u} \in \mathbb{U}, \tag{19a}$$

$$a(\boldsymbol{u}^{\text{p}}, \delta\boldsymbol{u}) = b(\epsilon^{\text{p}}, \delta\boldsymbol{u}) \quad \forall\delta\boldsymbol{u} \in \mathbb{U}. \tag{19b}$$

This separation simplifies the analysis.

4.2. Displacement field - PGD approximation

Solving for the displacement field in 3D is computationally expensive. To address this, the PGD method is used. In this case, PGD is used for a spatial domain decomposition $(\boldsymbol{y}, x)$. Thus, the 3D deformations are divided into simpler in-plane $\boldsymbol{y} = (y, z) \in \hat{\Omega}$ and out-of-plane $x \in I_x$ components. This approach has been extensively discussed in solving the linear elastic problem in our previous work [36], represented by $\boldsymbol{u}^{\text{e}}$ in (19a). In that paper, it was demonstrated how the PGD approximation can be extended to also include a large number of load parameters for complex loading. In what follows, we describe how this domain decomposition is used to solve for the permanent deformation $\boldsymbol{u}^{\text{p}}$ in (19b), applying the same PGD methodology.

The separated representation of $\boldsymbol{u}^{\text{p}}$ with respect to $\boldsymbol{y}$ and x is expressed as

$$\boldsymbol{u}^{\text{p}}(\boldsymbol{y}, x) \approx \boldsymbol{u}_{N}^{\text{PGD}}(\boldsymbol{y}, x) = \sum_{n=1}^{N} \boldsymbol{Y}_{n}(\boldsymbol{y}) \, X_{n}(x), \tag{20}$$

where the approximation $\boldsymbol{u}_{N}^{\text{PGD}}(\boldsymbol{y}, x)$ improves as N increases. Here, $\boldsymbol{Y}_{n}(\boldsymbol{y})$ and $X_{n}(x)$ represent the unknown separated functions for the nth mode and depend on the parameters in plane $\boldsymbol{y}$ and out-of-plane x, respectively.

Assuming the first $N - 1$ terms have already been computed, we seek to enrich the PGD solution by computing the modes $\boldsymbol{Y}_{N}(\boldsymbol{y}) \in \mathbb{Y}$ and $X_{N}(x) \in \mathbb{X}$

$$\boldsymbol{u}_{N}^{\text{PGD}}(\boldsymbol{y}, x) = \boldsymbol{u}_{N-1}^{\text{PGD}}(\boldsymbol{y}, x) + \boldsymbol{Y}_{N}(\boldsymbol{y}) \, X_{N}(x), \quad \boldsymbol{u}_{N-1}^{\text{PGD}}(\boldsymbol{y}, x) = \sum_{n=1}^{N-1} \boldsymbol{Y}_{n}(\boldsymbol{y}) \, X_{n}(x), \tag{21}$$

where $\mathbb{Y}$ and $\mathbb{X}$ are the function spaces defined as

$$\mathbb{Y} := \{\boldsymbol{v} \in [\mathbb{H}^{1}(\hat{\Omega})]^{3}, : \boldsymbol{v} = \boldsymbol{0} \text{ on } \hat{\Gamma}_{\text{D}}\}, \quad \mathbb{X} := \mathbb{H}^{1}(I_x), \tag{22}$$

Also, we note that any product $\boldsymbol{Y}_{n} X_{n} \in \mathbb{U}$.

The representation of $a(\boldsymbol{u}^{\text{p}}, \delta\boldsymbol{u})$ and $b(\epsilon^{\text{p}}, \delta\boldsymbol{u})$ from (13), (14) and (19b) is separated as

$$a(\boldsymbol{u}^{\text{p}}, \delta\boldsymbol{u}) = \int_{I_x} \int_{\hat{\Omega}} \epsilon[\delta\boldsymbol{u}] : \mathbf{E} : \epsilon[\boldsymbol{u}^{\text{p}}] \, d\hat{\Omega} \, dx, \quad b(\epsilon^{\text{p}}, \delta\boldsymbol{u}) = \int_{I_x} \int_{\hat{\Omega}} \epsilon[\delta\boldsymbol{u}] : \mathbf{E} : \epsilon^{\text{p}} \, d\hat{\Omega} \, dx. \tag{23}$$

with constrained displacements at $\hat{\Gamma}_D$.

The Galerkin method is used to establish the equations for determining the modes Y_N and X_N with $\delta u(y,x) = \delta u^{\mathrm{PGD}}(y,x) = \delta Y(y) X_N(x) + Y_N(y) \delta X(x)$ for $\delta Y, \delta X \in \mathbb{Y} \times \mathbb{X}$. Thus, inserting the PGD approximation (20) into (19b) we obtain the problem of seeking $Y_N, X_N \in \mathbb{Y} \times \mathbb{X}$ such that

$$a(Y_N X_N, \delta Y X_N) = b(\epsilon^p, \delta Y X_N) - a(u_{N-1}^{\mathrm{PGD}}, \delta Y X_N) \quad \forall \delta Y \in \mathbb{Y}, \tag{24a}$$

$$a(Y_N X_N, Y_N \delta X) = b(\epsilon^p, Y_N \delta X) - a(u_{N-1}^{\mathrm{PGD}}, Y_N \delta X) \quad \forall \delta X \in \mathbb{X}. \tag{24b}$$

Finally, the strain can be separated as

$$\epsilon[u^{\mathrm{PGD}}(y,x)] = \sum_{n=1}^{N} \hat{\epsilon}[Y_n(y)] X_n(x) + \epsilon_{\mathrm{X}}[Y_n(y)] \frac{dX_n(x)}{dx}, \tag{25}$$

where $\hat{\epsilon}[Y(y)] := [Y(y) \otimes \hat{\nabla}]^{\mathrm{sym}}$, $\epsilon_{\mathrm{X}}[Y(y)] := [Y(y) \otimes e_x]^{\mathrm{sym}}$ and $\hat{\nabla} = [I - e_x \otimes e_x]$ is the projection of the in-plane gradient ∇. This separation allows us to solve a 2D and 1D problem separately instead of the full 3D problem. A more detailed description of the separated representation and the matrix structure of the problem is presented in Appendix A.

4.3. Integration of flow rule and back stresses along streamlines

In order to integrate the evolution rules in (16), spatial integration is considered along the streamlines for each given displacement field u. In the prismatic mesh, the streamlines $k = (1, 2, \ldots, K_{\hat{\Omega}})$ are defined through the quadrature points y_k in the cross section $\hat{\Omega}$. Each streamline in the out-of-plane interval I_x is discretized into N discrete points, $x_1 > x_2 > \cdots > x_N$, where each point corresponds to a Gauss point pertinent to the finite element discretization of I_x. The integration points are defined from the right as shown in Fig. 4. In addition, $x_0 = d/2$ corresponds to the inlet boundary condition, ϵ_{in}^p and α_{in}^i, and the outlet values, $\epsilon_{\mathrm{out}}^p$ and α_{out}^i, are extracted at x_N. Due to the structured mesh in the x-direction, each streamline k shares the same discretization.
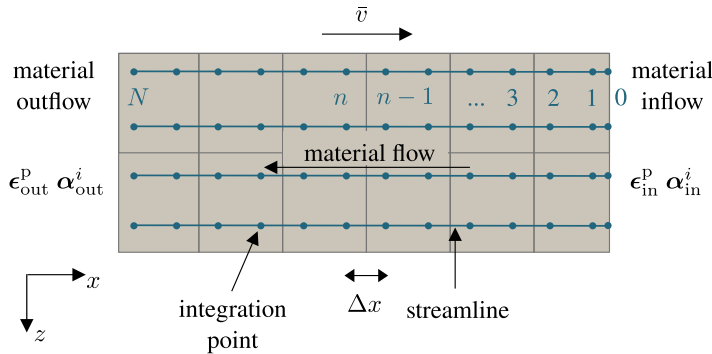
Fig. 4. Integration point numbering $n = (0, 1, 2, \ldots, N)$ along streamlines parallel to the x-axis from right to left, where $n = 0$ is the given initial condition ϵ_{in}^p, α_{in}^i and $n = (1, 2, \ldots, N)$ corresponds to the quadrature points. The integration points align with the Gauss points in the FE-mesh, and Δx defines the distance between the two points.

Applying the Backward Euler (BE) method to the discretized interval I_x in (16a) and (16b) yields the integrated flow rule as

$$-\bar{v} \frac{\partial \epsilon^p}{\partial x} \approx \frac{\bar{v}}{\Delta x} \left(\epsilon^p - {}^{n-1}\epsilon^p \right) = \lambda v \Rightarrow \epsilon^p = {}^{n-1}\epsilon^p + \mu v. \tag{26}$$

where $\epsilon^p = \epsilon^p(y_k, x_n)$ and ${}^{n-1}\epsilon^p = \epsilon^p(y_k, x_{n-1})$ for streamline k. Moreover, $\Delta x = (x_n - x_{n-1})$, and we introduce the re-scaled BE-integrated plastic multiplier $\mu = \frac{\Delta x}{\bar{v}} \lambda$. Similarly, the integrated back-stresses are integrated as

$$\alpha^i = {}^{n-1}\alpha + \frac{2}{3} C_i \mu v - \frac{\gamma_i^{m_i+1}}{3} \alpha_e^{i,m_i} < \mu v : \alpha^i > \frac{\alpha^i}{\alpha_e^i}. \tag{27}$$

where $\alpha^i = \alpha^i(y_k, x_n)$ and ${}^{n-1}\alpha^i = \alpha^i(y_k, x_{n-1})$.

In (26) and (27), we note that $v = v(\epsilon, \epsilon^p, \alpha^i)$ from (5a) is considered at (y_k, x_n), and the Kuhn Tucker conditions are evaluated at the current integration point, i.e., $\Phi(\epsilon, \epsilon^p, \alpha^i) \leq 0$, $\mu \geq 0$, $\mu \Phi = 0$.

In the case of plastic loading, i.e., $\Phi\left[\sigma^{\mathrm{tr}}, {}^{n-1}\alpha^i\right] > 0$, and from $\sigma = E : (\epsilon - \epsilon^p)$, we obtain the integrated stresses for a specific streamline between two out-of-plane integration points as

$$R_\sigma(\sigma, \mu) = \sigma - \sigma^{\mathrm{tr}} + \mu E : v = 0, \quad \sigma^{\mathrm{tr}} := E : (\epsilon[u] - {}^{n-1}\epsilon^p), \tag{28a}$$

$$R_\alpha(\alpha^i, \mu) = \alpha^i - {}^{n-1}\alpha^i - \frac{2}{3} C_i \mu v + \frac{\gamma_i^{m_i+1}}{C_i^{m_i}} \alpha_e^{m_i} < \mu v : {}^n\alpha^i > \frac{\alpha^i}{\alpha_e} = 0, \tag{28b}$$

$$R_\mu(\boldsymbol{\sigma}, \boldsymbol{\alpha}^i) = \Phi = 0, \tag{28c}$$

where the trial stress $\boldsymbol{\sigma}^{\mathrm{tr}}$ corresponds to fixed plastic strain at x_{n-1}. The integrated stresses $\{\boldsymbol{\sigma}, \boldsymbol{\alpha}^i, \mu\}$ are computed iteratively using Newton's method for a given displacement $\boldsymbol{u}$ and with initial conditions $\epsilon_{\mathrm{in}}^{\mathrm{p}}(\boldsymbol{y}_k)$ and $\boldsymbol{\alpha}_{\mathrm{in}}^i(\boldsymbol{y}_k)$, which are defined at each streamline $\{\boldsymbol{y}_k\}_{k=1}^{K_{\hat{\Omega}}}$ in the cross-section $\hat{\Omega}$. Details of the iterative procedure are provided in Appendix B.

In summary, the evolution equations can be compactly expressed as

$$[\epsilon^{\mathrm{p}}(\boldsymbol{y}, x), \boldsymbol{\alpha}^i(\boldsymbol{y}, x)] = f\left(\boldsymbol{\epsilon}[\boldsymbol{u}](\boldsymbol{y}, x), \epsilon_{\mathrm{in}}^{\mathrm{p}}(\boldsymbol{y}), \boldsymbol{\alpha}_{\mathrm{in}}^i(\boldsymbol{y})\right), \tag{29}$$

where f represents the algorithmic (discrete) evolution in (26) and (27). These variables can be solved independently for each streamline in the cross-section, enabling parallelization to improve computational efficiency.

For increased accuracy, a finer discretization of I_x is used near the contact load, where larger changes in stresses and strains are expected rather than throughout the entire interval. Since the material response is strain-controlled in the trial stress, convergence is normally ensured for small step sizes. However, sub-incrimination is applied in a streamline k if the solution in an integration point x_n does not converge.

4.4. Fixed-point algorithm for elastic and plastic displacement fields

To efficiently manage the coupling between ϵ^{p} and $\boldsymbol{u}^{\mathrm{p}}$, we will alternate between solving (19b) and (29) with fixed-point iterations until convergence is achieved. An advantage of this approach is that it allows us to account for the inelastic material of the railhead without the need to update the tangent stiffness tensor during iterations, which reduces the computation time. We utilize fixed-point iterations rather than methods such as Newton or Newton–Raphson, to avoid computing the function's derivatives.

The iterative process alternates between updating $\epsilon^{\mathrm{p}(k)}$ in iteration k assuming that $\boldsymbol{u}^{\mathrm{p}(k-1)}$ is known and then updating $\boldsymbol{u}^{\mathrm{p}(k)}$ from $\epsilon^{\mathrm{p}(k)}$. The elastic displacement $\boldsymbol{u}^{\mathrm{e}}[{}^l\boldsymbol{q}]$ can be precomputed from (19a) for linear elastic material given a loading scenario ${}^l\boldsymbol{q}$. The elastic displacement can be determined either with a 3D FE solution or using PGD with a domain decomposition and a parameterization of the load as explained in [36].

Each iteration in the fixed-point algorithm consists of:

- Integration of $\epsilon^{\mathrm{p}(k)}$ and $\boldsymbol{\alpha}^i$ given $\boldsymbol{u}^{\mathrm{p}(k-1)}$, $\boldsymbol{u}^{\mathrm{e}}[{}^l\boldsymbol{q}]$, and the inflow of the material $\epsilon_{\mathrm{in}}^{\mathrm{p}}(\boldsymbol{y})$ and $\boldsymbol{\alpha}_{\mathrm{in}}^i(\boldsymbol{y})$ (see Section 3.2). This integration was formulated in (29) and is expressed as

$$[\epsilon^{\mathrm{p}(k)}(\boldsymbol{y}, x), \boldsymbol{\alpha}^i(\boldsymbol{y}, x)] = f\left(\boldsymbol{\epsilon}[\boldsymbol{u}^{\mathrm{e}}[\boldsymbol{q}] + \boldsymbol{u}^{\mathrm{p}(k-1)}](\boldsymbol{y}, x), \epsilon_{\mathrm{in}}^{\mathrm{p}}(\boldsymbol{y}), \boldsymbol{\alpha}_{\mathrm{in}}^i(\boldsymbol{y})\right). \tag{30}$$

- Computation of $\boldsymbol{u}^{\mathrm{p}(k)}$ from $\epsilon^{\mathrm{p}(k)}$, where (19b) is stated as

$$a(\boldsymbol{u}^{\mathrm{p}(k)}, \delta\boldsymbol{u}) = b(\epsilon^{\mathrm{p}(k)}, \delta\boldsymbol{u}) \quad \forall \delta\boldsymbol{u} \in \mathbb{U}. \tag{31}$$

It should be noted that: (1) the integration of plastic strains also gives ${}^l\epsilon_{\mathrm{out}}^{\mathrm{p}}$ and ${}^l\boldsymbol{\alpha}_{\mathrm{out}}^i$ after each over rolling, (2) $\epsilon^{\mathrm{p}(k)}$ and $\boldsymbol{\alpha}^i$ can be solved with parallel computation for each streamline in the cross-section as explained in Section 4.3, and (3) for a given $\epsilon^{\mathrm{p}(k)}$, the permanent displacement in (31) can be solved efficiently for a dimensional decomposition of $(\boldsymbol{y}, x)$ using PGD as outlined in Section 4.2 and Appendix A.

The fixed-point algorithm begins with an initial assumption for $\boldsymbol{u}^{\mathrm{p}}$ at $k = 1$, setting it to $\boldsymbol{u}^{\mathrm{p},(0)} = \boldsymbol{0}$ for the first over rolling. For the subsequent over rollings, we use the initial guess

$$\boldsymbol{u}^{\mathrm{p},(0)}(\boldsymbol{y}, x) = {}^{l-1}\boldsymbol{u}^{\mathrm{p}}(\boldsymbol{y}, -d/2) \quad (\boldsymbol{y}, x) \in \hat{\Omega} \times I_x. \tag{32}$$

Here, ${}^{l-1}\boldsymbol{u}^{\mathrm{p}}(\boldsymbol{y}, -d/2)$ is the resulting displacement field after the prescribed load passage. Using the uniform extension in I_x ensures[1] consistency for zero external loads.

Each over rolling requires several fixed-point iterations to converge. The iterations continue until the residual Δ is smaller than a user-specified tolerance ϵ. The residual represents the norm of incremental permanent displacement change between two iterations $\boldsymbol{\phi}^{(k)}$ as

$$\boldsymbol{\phi}^{(k)} = \boldsymbol{u}^{\mathrm{p}(k)} - \boldsymbol{u}^{\mathrm{p}(k-1)}, \tag{33a}$$

$$\Delta = \frac{\|\boldsymbol{\phi}^{(k)}\|}{\sqrt{\|\boldsymbol{\phi}^{(1)}\|^2 + \|\boldsymbol{u}^{\mathrm{p},(0)}\|^2}}. \tag{33b}$$

In practice, the L_2 norm of the functions is replaced with the Euclidean norm of the nodal vector. Specifically, for the functional values of $\boldsymbol{u}$, the nodal vector norm is calculated as $\|\boldsymbol{u}\| \to |\underline{\boldsymbol{u}}| = \sqrt{\sum_{k=1}^N u_k^2}$. The residual is divided with the start guess $\boldsymbol{u}^{\mathrm{p},(0)}$ and first iteration $\boldsymbol{u}^{\mathrm{p},(1)}$ to get a normalized value. This indicator for convergence monitoring is chosen because negligible changes in permanent deformation between iterations signify convergence.

The algorithmic implementation for the ROM framework is summarized in the flow chart shown in Fig. 5.

---

[1] This would formally require $d/2 \to \infty$, i.e., where there is no remaining elastic deformation at the truncated inflow boundary.
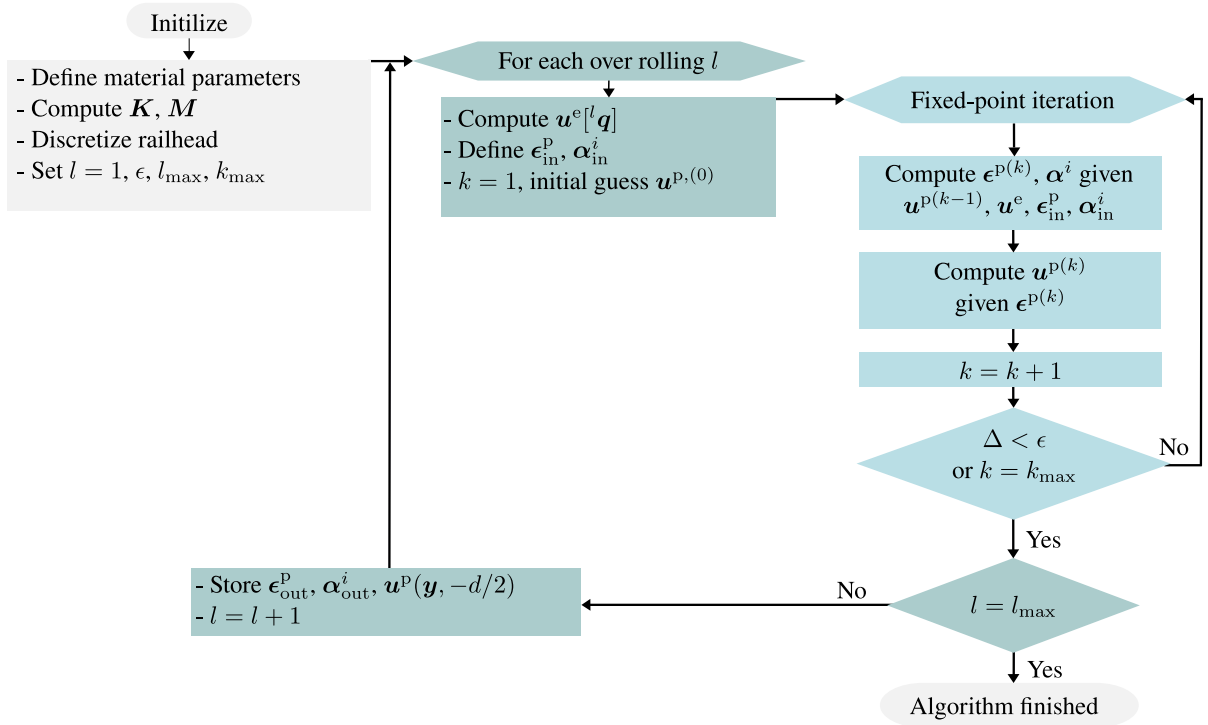
Fig. 5. Algorithmic implementation of the ROM framework, evaluated for over rollings in the load collective $l_{\max}$. The fixed-point iteration continues until convergence $\Delta < \epsilon$ or the number of iterations $k_{\max}$ is reached.

5. Verification against reference FE solution

To validate the accuracy and highlight the computational time of the ROM framework implemented in an in-house code in MATLAB, the results are compared with those obtained from a 3D FE model. The 3D FE model simulated a moving contact load and is based on the momentum balance described in Section 2.1. The 3D FE simulations are carried out using the commercial software ABAQUS.

5.1. Problem setup

5.1.1. Material model

Both analyzes consider the properties of the elastic–plastic material of the railhead, described by the Ohno–Wang material model [42], as explained in Section 2.2. The material model is calibrated against experimental data controlled by uniaxial stress of R260 rail grade material from Ahlström et al. [44]. The identified material parameters, including three back-stresses ($n_b = 3$), are listed in Table 1. The material routine is implemented in Fortran and integrated into Abaqus as a user material subroutine (UMAT). For the ROM framework implementation in MATLAB, the routine is compiled with a MEX function, enabling faster computation. Section 4.3 details the integrated plastic response. It is emphasized that the (standard) temporal integration in the reference model directly carries over to the convected formulation in the ROM simply by changing the timestep Δt to the spatial step $\Delta x / \bar{v}$.

Table 1
Calibrated material parameter values for the Ohno–Wang model [42] for the rail grade R260.

Description	Symbol	Value
Elastic modulus	E	200 GPa
Poisson's ratio	v	0.3
Yield limit	σ_y	295 MPa
Kinematic hardening modulus	C	[492.2, 37.5, 2.5] GPa
Material parameter	γ	[3929, 156, 0]
Multiplier	m	[1.59, 2.97, 1] MPa

5.1.2. Mesh configuration

The 3D railhead in both analyzes is modeled according to a measured UI60 railhead profile, as shown in Fig. 6. The results are evaluated in the middle part of the railhead with a depth of $d_m = 100$ mm (highlighted in blue in the Figure) to minimize

boundary effects. Both the ROM framework and the reference model use the same mesh configuration with wedge elements of $762 \times 50 = 22{,}860$ Degrees Of Freedom (DOF). This mesh allows for direct comparisons, although it is better suited for ROM. It requires fine discretization for both methods, especially near the contact region, to accurately capture stress and strain gradients. For the reference solution, this necessitates fine discretization in the contact region along the entire length of the railhead, thus leading to longer simulation times.

(a) *Reference model, $d = 150$ mm*   **(b)** *ROM framework, $d = 200$ mm*   **(c)** *Domain decomposition*
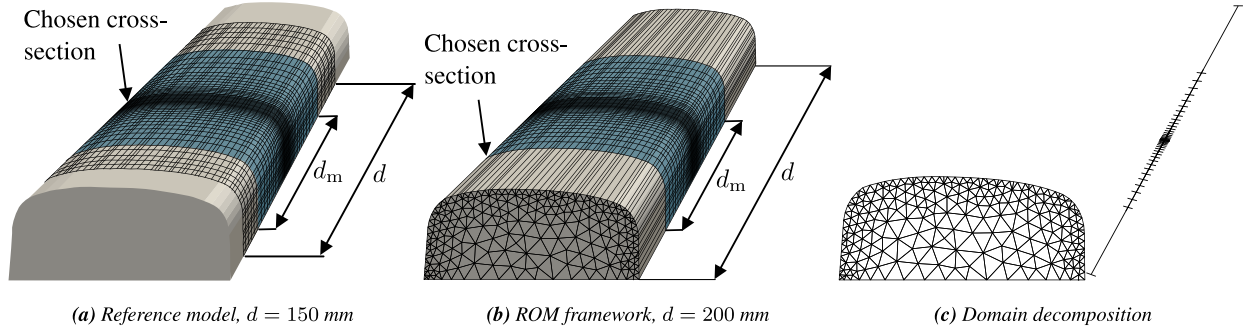
Fig. 6. Mesh for (a) the reference model, (b) the ROM framework, and (c) the domain decomposition used for computing the permanent displacement field in the ROM. The midsection, $d_\mathrm{m} = 100$ mm, is highlighted in blue in (a) and (b). Results are evaluated for a chosen cross-section, (a) at the middle, and (b) at the front. (For interpretation of the references to color in this figure legend, the reader is referred to the web version of this article.)

To account for the influence of contact loads, the models extend beyond the midsection of the railhead. Different lengths d for the ROM and reference solutions are considered, as illustrated in Fig. 6. In the ROM framework, a length of $d = 200$ mm is used. This model requires only one additional row of wedge elements on each side of the midsection to mitigate the boundary effects due to the stationary contact load, resulting in $762 \times 52 = 39{,}624$ DOF in total. On the other hand, the reference model uses a shorter length of $d = 150$ mm to balance the computation time and the accuracy of the solution. Longer rails require more time increments due to the longer rolling distance and larger DOF in the case of moving contact loads. More wedge elements are needed outside the midsection to prevent an overly stiff response, with a wedge element length chosen of 5 mm for the outer regions. This configuration results in $762 \times 60 = 45{,}720$ DOF in the reference model.

To save computational time while maintaining accuracy, the computation of the permanent displacement field $\boldsymbol{u}^\mathrm{p}$ is performed using the domain decomposition with the PGD method explained in Section 4.2. The PGD solution comprises an equivalent discretization with 762 in-plane DOF and 52 out-of-plane DOF, as seen in Fig. 6c. In-plane, 3-noded triangular elements with linear shape functions are used, while 1D linear elements are used out-of-plane. When computing $\boldsymbol{u}^\mathrm{p}$, the tolerance in the PGD solution is set to $\epsilon_\mathrm{PGD} = 1 \times 10^{-2}$, not to confuse with ϵ in Section 4.4. Refer to Appendix A for the definition of the convergence criterion.

5.1.3. Contact load scenario

The contact scenario is defined by a Hertz distributed load [41], $\boldsymbol{q} = (s, a, b, p_\mathrm{n}, p_\mathrm{t}, p_\mathrm{x})$, as illustrated in Fig. 2. The load is placed in the middle of the railhead ($s = 0$ mm) with a semi-axis length of $a = b = 10$ mm. To assess the ROM's capability to model the response from various load scenarios, three different traction setups are investigated:

1. Normal and lateral (peak) surface contact traction $[p_\mathrm{n}, p_\mathrm{t}, p_\mathrm{x}] = [1.2, -0.3, 0]$ GPa.
2. Normal and longitudinal (peak) surface contact traction, $[p_\mathrm{n}, p_\mathrm{t}, p_\mathrm{x}] = [1.2, 0, 0.3]$ GPa.
3. (Peak) traction applied in all directions $[p_\mathrm{n}, p_\mathrm{t}, p_\mathrm{x}] = [1.2, -0.3, 0.3]$ GPa.

The elastic displacement $\boldsymbol{u}^\mathrm{e}[\boldsymbol{q}]$ is precalculated from a given load scenario in the ROM framework. To identify the accuracy of the fixed-point procedure without the domain decomposition affecting the solution, a 3D FE solution is used as explained in [36].

5.2. Single over rolling

In this Section, the response for a single over rolling is compared between the ROM framework and the reference case in terms of convergence, CPU time, and permanent displacement field for the different load cases mentioned in Section 5.1.3.

5.2.1. Residual and displacement error

To evaluate the accuracy of the displacement response in the ROM solution, the number of fixed-point iterations needed to reach a certain displacement error is analyzed. Fig. 7a presents the relative error e in the permanent deformation of the railhead profile when comparing the solutions. Fig. 7b illustrates the residual Δ after each fixed-point iteration, as given in (33b). The relative error e is defined as

$$e = \frac{|{}^\mathrm{prof}\underline{\boldsymbol{u}}^\mathrm{p}_\mathrm{REF} - {}^\mathrm{prof}\underline{\boldsymbol{u}}^\mathrm{p}_\mathrm{ROM}|}{|{}^\mathrm{prof}\underline{\boldsymbol{u}}^\mathrm{p}_\mathrm{ROM}|}, \tag{34}$$

where ${}^{\text{prof}}\underline{\boldsymbol{u}}^{\text{p}}_{\text{REF}}$ and ${}^{\text{prof}}\underline{\boldsymbol{u}}^{\text{p}}_{\text{ROM}}$ are the nodal displacement pertinent to nodes on the top of the rail profile ($\hat{\varGamma}_N$) for a chosen cross-section of the models defined in Fig. 6.

The figures show a gradual improvement in the accuracy of the solution as more fixed-point iterations are carried out (see Fig. 7a). The accuracy reaches a plateau after approximately 15–30 iterations, depending on the load case. At this point, $\varDelta < 5 \times 10^{-3}$ (see Fig. 7b), which provides a tolerance level for the results presented. At that point, the PGD solution can accurately capture the displacement field with a relative displacement error of 0.1 (see Fig. 7a).
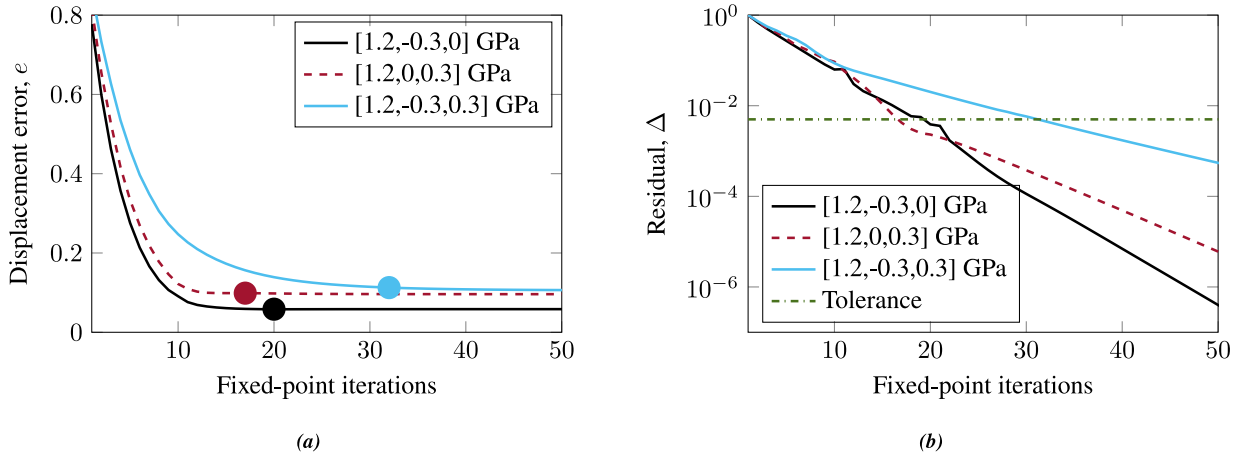
Fig. 7. Relationship between iterations and (a) relative displacement error e defined in (34), and (b) residual $\varDelta$ defined in (33b), for different load cases. In (a), the dots show the displacement error when $\varDelta < 5 \times 10^{-3}$.

5.2.2. Computational time

When comparing the Central Processing Unit (CPU) time, the ROM is significantly more computationally efficient than the reference analysis. Both simulations were executed on a computer cluster using 20 cores of an Intel Xeon Gold 6130 ("Skylake") CPU and 96 GB of RAM [45]. Depending on the load case, the reference solution typically requires 3000 to 5000 s to complete a single over rolling simulation. In contrast, the CPU time for the ROM, specifically fixed-point iterations, is shown in Fig. 8. Each fixed-point iteration takes around 2.3 s, most of that time coming from the computation of the plastic strains in the railhead part. It is important to note that the CPU time excludes the time needed to establish a parallel pool in MATLAB, which is approximately 84 s. However, this pool is established only for the first over rolling. Even when this time is included, obtaining the response from one over rolling using the ROM framework is significantly faster than in the reference case. For the loading scenario $[p_{\text{n}}, p_{\text{t}}, p_{\text{x}}] = [1.2, -0.3, 0.3]$ GPa, the CPU time is 4631 s the reference case and 73 s (not including the time to open the parallel pool) in the ROM for a total of 32 fixed-point iterations, making the computation 63 times faster.
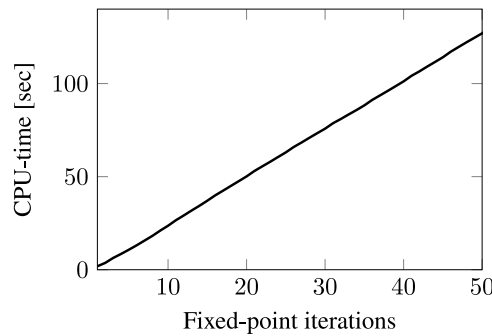
Fig. 8. CPU-time for the fixed-point iterations for the ROM solution.

5.2.3. Displacement field

Fig. 9 displays the 3D displacement field $\boldsymbol{u}^{\text{p}} + \boldsymbol{u}^{\text{e}}$ in the middle section of the railhead (see Fig. 6) for the stationary rolling contact load condition after a single over rolling, with the residual satisfying the chosen tolerance. The maximum displacement occurs in the middle of the railhead where the load is applied, and the front of the railhead displays the permanent deformation that remains after the contact load's passage.

(a) $[1.2, -0.3, 0]$ *GPa*   **(b)** $[1.2, 0, 0.3]$ *GPa*   **(c)** $[1.2, -0.3, 0.3]$ *GPa*
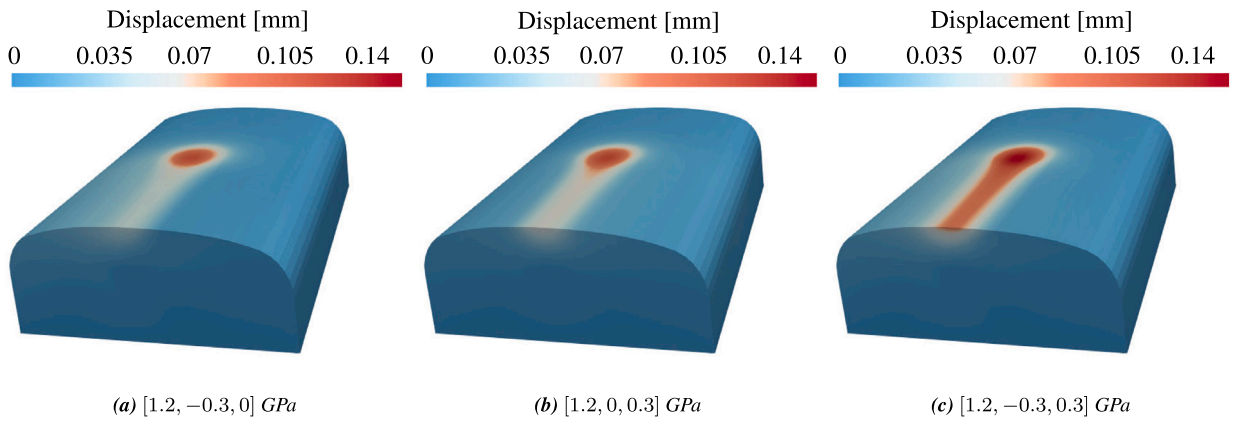
Fig. 9. Norm of displacement field in the ROM solution for different load setups of $[p_n, p_t, p_x]$.

Figs. 10a, 11a and 12a illustrate a comparison of the ROM solution with the reference case in terms of vertical displacement along a surface line throughout the railhead for the three different load cases described in Section 5.1.3. The reference case uses conventional FEM to solve the moving contact load problem, with results extracted when the contact load is at the middle and end of the rail. These cases are labeled "Reference" and "Ref. over rolling", respectively, in the Figures. Hence, "Reference" represents the displacement under the moving load and "Ref. over rolling" the remaining displacement after over rolling. The vertical displacement in the non-linear ROM is well-matched to the reference solution. A slight discrepancy in vertical displacement can be observed in the reference solution after the complete passage of the moving contact load, attributed to the discretization of the railhead model.

Figs. 10b, 11b and 12b show the permanently deformed railhead profile, with the deformation scaled by a factor of 200, for a cross-section in both the ROM and reference case. Three cross-sections are chosen for the reference case post-over rolling to illustrate the variation throughout the railhead. Given the correspondence of the solutions, we thus conclude that the ROM solution is suitable for accurately evaluating the plasticity-induced deformation of the railhead from over rolling.

(a)   **(b)**
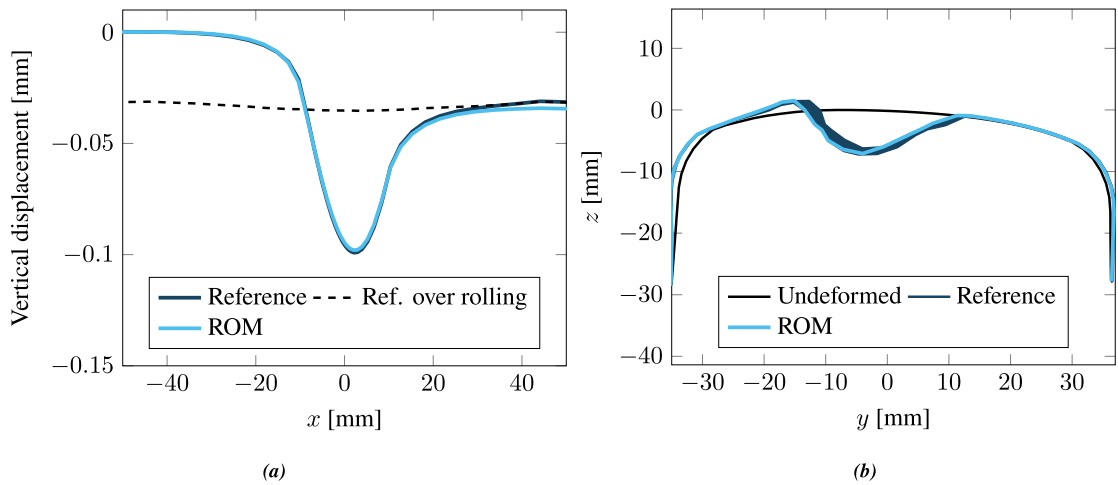
Fig. 10. Displacement for $[p_n, p_t, p_x] = [1.2, -0.3, 0]$ GPa. (a) Vertical displacement along a line at the railhead surface, and (b) cross-section of the railhead profile in its undeformed and deformed state, the deformation is scaled by a factor of 200.
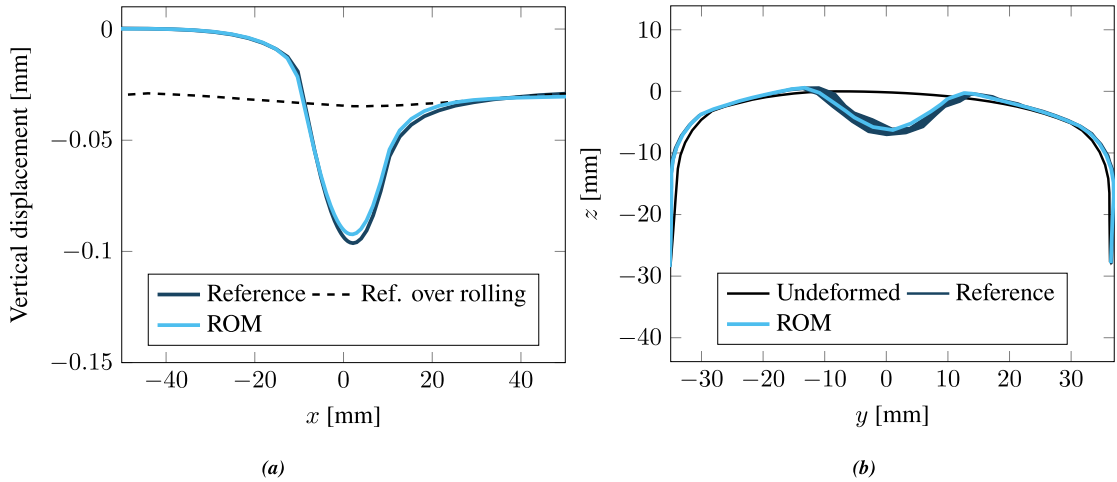
Fig. 11. Displacement for $[p_n, p_t, p_x] = [1.2, 0, 0.3]$ GPa. (a) Vertical displacement along a line at the railhead surface, and (b) cross-section of the railhead profile in its undeformed and deformed state, the deformation is scaled by a factor of 200.
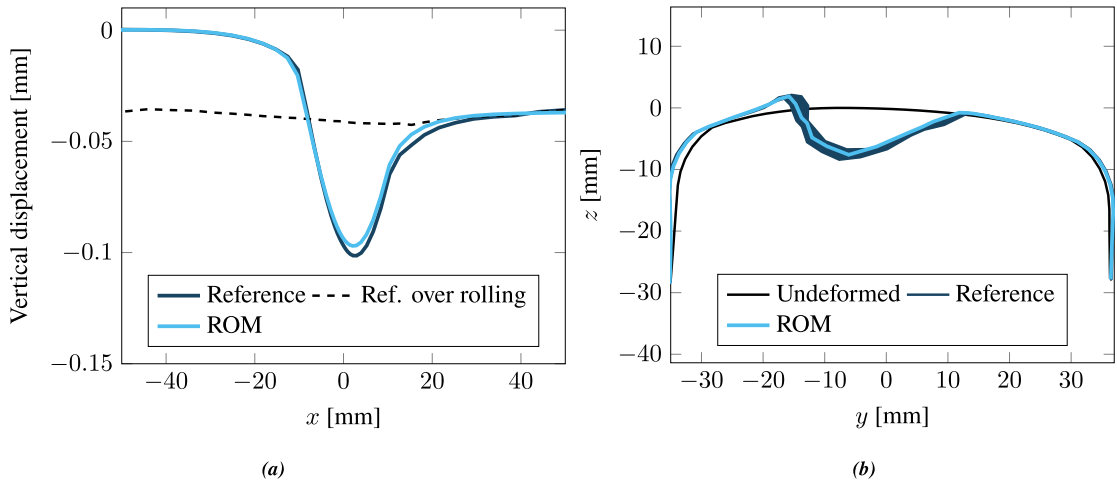
Fig. 12. Displacement for $[p_n, p_t, p_x] = [1.2, -0.3, 0.3]$ GPa. (a) Vertical displacement along a line at the railhead surface, and (b) cross-section of the railhead profile in its undeformed and deformed state, the deformation is scaled by a factor of 200.

5.2.4. Effect of load magnitude on convergence

To evaluate the robustness of ROM, the convergence behavior of the residual Δ is investigated under varying load magnitudes for the Ohno–Wang and linear hardening material models. The latter is a simpler isotropic hardening model with a hardening modulus of $H = E/10$. Specifically, the convergence is assessed by scaling one of the load scenarios, $[p_n, p_t, p_x] = [1.2, -0.3, 0.3]$ GPa, with a load amplitude factor λ. Fig. 13 illustrates the effect of this scaling on the convergence of Δ for $\epsilon = 5 \times 10^{-2}$. As the load amplitude increases, the convergence rate decreases. Notably, for $\lambda = 1.5$, the ROM does not converge when using the Ohno–Wang material model (marked with an "X" in the figure), while the linear hardening model maintains convergence. This suggests that the hardening within the Ohno–Wang model becomes saturated at higher load levels.

5.3. Multiple load passages

To further validate our ROM, multiple load passages were simulated using the Ohno–Wang plasticity model, with a residual tolerance, defined in Section 4.4, of $\epsilon = 5 \times 10^{-3}$. The material model and mesh settings described in Sections 5.1.1 and 5.1.2 were used, including the three different load scenarios described in Section 5.1.3. The following sections present the results obtained for the load cases applied repeatedly.
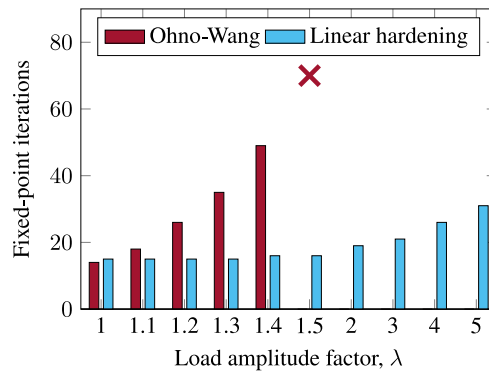
Fig. 13. How the load scale amplitude λ affects the convergence of $\Delta < 5\times10^{-2}$ for load case $[p_n, p_t, p_x] = [1.2, -0.3, 0.3]$ GPa. The "X" indicates that no convergence was reached at $\lambda = 1.5$ for the Ohno–Wang plasticity model.

5.3.1. Number of fixed-point iterations

Fig. 14 illustrates the number of fixed-point iterations required to achieve convergence in the load case $[p_n, p_t, p_x] = [1.2, -0.3, 0.3]$ GPa. The iterations decrease to find a converged solution as more over rollings are simulated. This reduction occurs because the plastic zone stabilizes and the hardening of the material becomes saturated for successive over rollings for the load case considered.
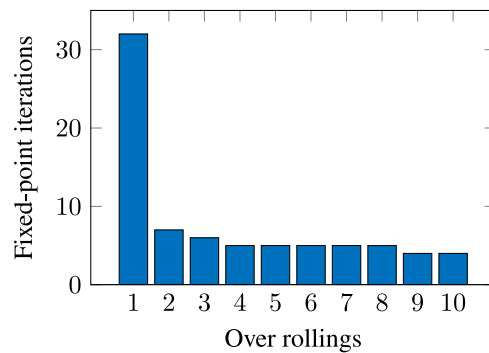
Fig. 14. Number of fixed-point iterations needed to reach convergence $\Delta < 5 \times 10^{-3}$ for ten over rollings of load case $[p_n, p_t, p_x] = [1.2, -0.3, 0.3]$ GPa.

5.3.2. Computational time

Fig. 15 shows the CPU time for the ROM and the reference solution for multiple over rollings. The ROM requires significantly less computational time. The initial over rolling takes 73 s (excluding the time to open the parallel pool), with each subsequent one taking less time due to fewer fixed-point iterations needed for convergence, as illustrated in Fig. 14. In contrast, the reference solution takes much longer for each over rolling due to the multiple load increments applied, resulting in consistent but extended computational times.
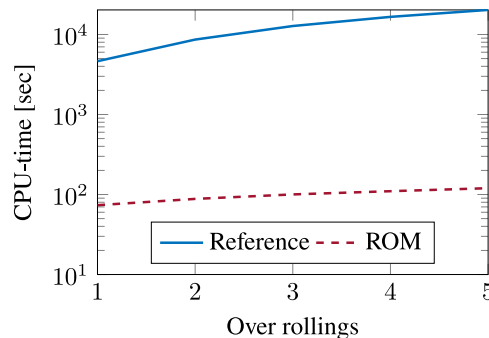
Fig. 15. CPU-time after each over rolling for the ROM and the reference solution.

5.3.3. Displacement field

Figs. 16 to 17 display the displacement field for multiple load passages. Fig. 16a compares the L_2 norm of the permanent profile displacement for a railhead cross-section after each over rolling, considering the three different load scenarios. It is evident that the ROM effectively captures the permanent displacement. Fig. 16b shows the 3D displacement field after five over rollings for the load case $[p_n, p_t, p_x] = [1.2, -0.3, 0.3]$ GPa, revealing permanent deformation along the entire railhead compared to when only one over rolling in Fig. 9 was considered.
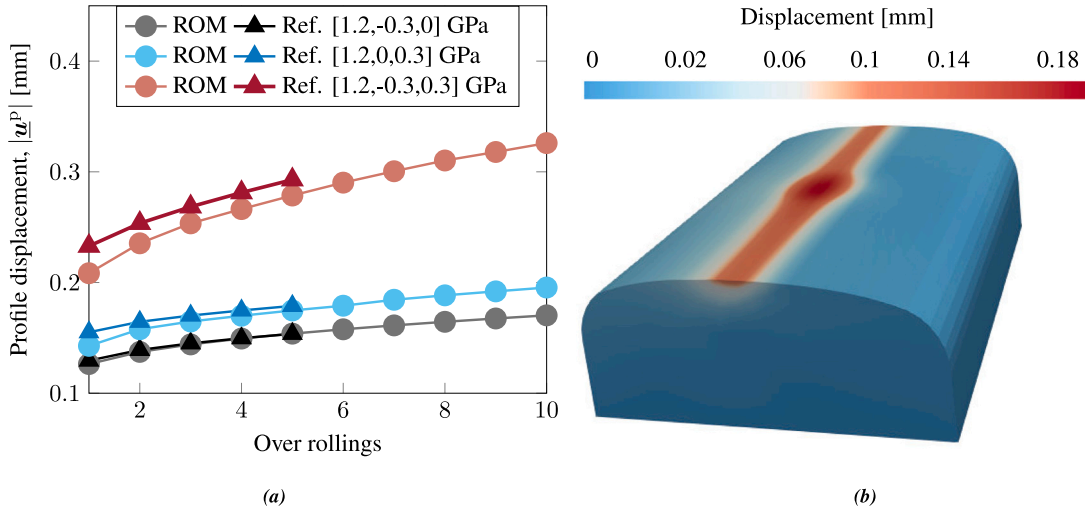
Fig. 16. (a) Norm of nodal displacement vector of the permanent profile after each over rolling for the ROM and reference solution. (b) Norm of displacement field in the ROM solution after five over rollings.

Fig. 17a presents the vertical displacement for a line along the railhead surface for the load case $[p_n, p_t, p_x] = [1.2, -0.3, 0.3]$ GPa. Fig. 17b shows the permanently deformed railhead profile after one and five over rollings for the ROM and the reference solution. The results are similar, especially after five over rollings, indicating the ROM's robustness and accuracy in capturing railhead deformation for repeated over rollings.
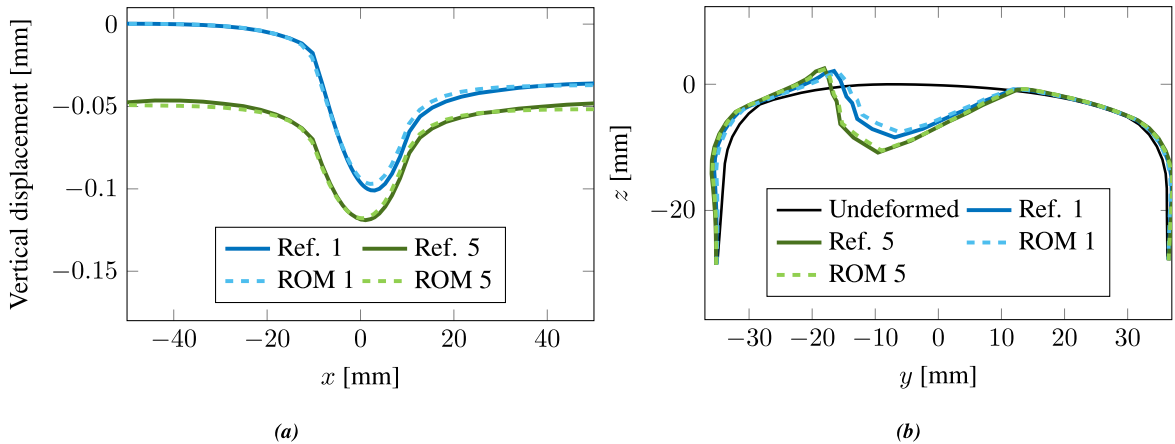
Fig. 17. Displacement for $[p_n, p_t, p_x] = [1.2, -0.3, 0.3]$ GPa after the first and fifth over rolling. (a) Vertical displacement along a line at the railhead surface, and (b) cross-section of the railhead profile before and after it has been deformed, the deformation is scaled by a factor of 200.

6. Evolving plasticity under varied hertzian contact load scenarios

To demonstrate the potential of our ROM, the response from different contact load scenarios was simulated while keeping the mesh and material settings from Section 5. The load collective of 100 different contact scenarios was generated based on multibody simulations of the dynamic vehicle-track interaction for a given traffic scenario described in [5]. The residual tolerance, defined in Section 4.4, was set to $\epsilon = 1 \times 10^{-2}$. In total, it takes 36 min to generate the plasticity response for the entire load collective.

Fig. 18a shows the number of fixed-point iterations required to achieve convergence in each over rolling. Consistent with Fig. 14, the general trend indicates that fewer iterations are needed for subsequent over rollings as the material hardens, or for lower traction magnitudes.
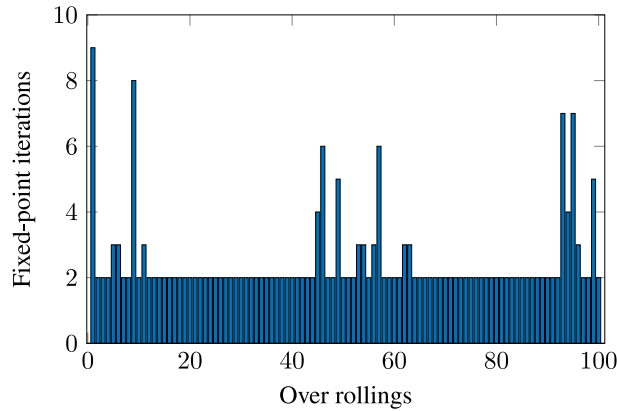
Fig. 18. Number of fixed-point iterations for the load collective to achieve convergence $\Delta < 1 \times 10^{-2}$.

Fig. 19a shows the Euclidean norm of the permanent profile displacement for a cross-section of the railhead profile after each over rolling. For some over rollings, this value is constant, indicating that some load scenarios do not result in any plastic deformation. Fig. 19b displays the cross-section of the deformed railhead profile for the entire load collective, with the deformation scaled by a factor of 400. It can be seen how the shift in contact location results in the geometry of the railhead evolving at various points along the profile.

(a)

(b)
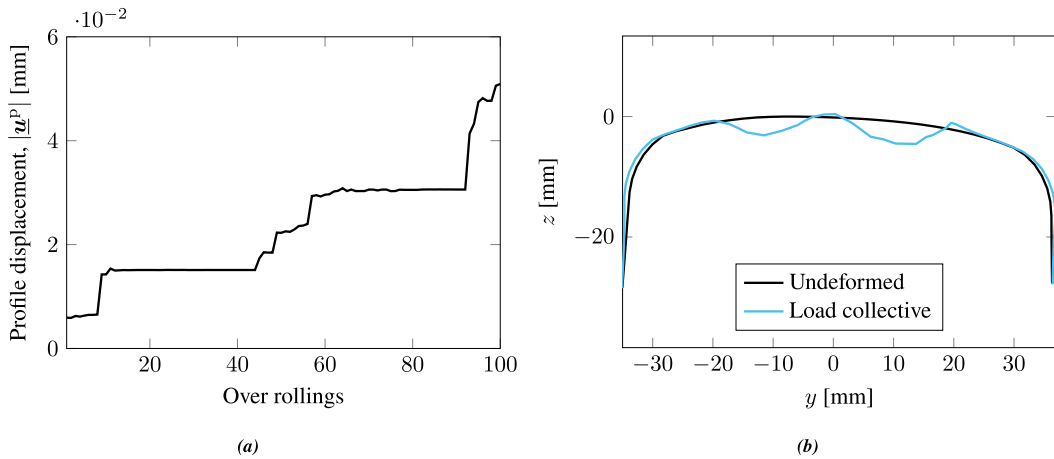
Fig. 19. (a) Norm of nodal displacement vector of the permanent profile per over rolling. (b) Displacement field for the entire load collective, the deformation is scaled by a factor of 400.

7. Conclusion

In this paper, we have developed a Reduced-Order Model (ROM) framework to efficiently solve the evolving plasticity in a three-dimensional railhead in various wheel-rail contact scenarios. Our approach assumes a stationary contact problem for a single over rolling for a convective coordinate system along the railhead. In addition, fixed-point iterations are used to solve for plastic strains from the displacement field and the displacements caused by given loading scenarios and plastic strains. The displacement field is solved using Proper Generalized Decomposition (PGD) for spatial domain decomposition. The response of the strain-controlled material ensures the convergence of the material routine, and parallel computations are used to increase the computational efficiency.

Comparisons between the ROM framework and a 3D finite element reference solution for a moving contact load show high accuracy for both a single over rolling and multiple over rollings when comparing the displacement fields. Moreover, our non-linear ROM formulation significantly reduces the computational cost, making it suitable for computing the accumulated plastic deformation for many over rollings under different contact load scenarios.

Future work aims to integrate this ROM into existing simulation frameworks from [5] to accurately capture the evolution of plasticity in rails, especially to efficiently predict long-term damage. Further research suggests using this ROM framework to predict the development of fatigue cracks in rolling contact and the crack direction initiation. Another possible extension is to use this framework to develop advanced models for contact formulation, i.e., to determine the load distribution from the simulation of the wheel–rail contact. If inertial terms or transient loads are to be considered, the solution will need to be expanded to include a time-dependent component.

CRediT authorship contribution statement

Caroline Ansin: Writing – review & editing, Writing – original draft, Visualization, Validation, Project administration, Methodology, Investigation, Formal analysis, Conceptualization. **Fredrik Larsson:** Writing – review & editing, Project administration, Methodology, Funding acquisition, Formal analysis, Conceptualization. **Ragnar Larsson:** Writing – review & editing, Investigation.

Declaration of competing interest

The authors declare that they have no known competing financial interests or personal relationships that could have appeared to influence the work reported in this paper.

Acknowledgments

Appendix A. Separated representation

This Section gives a detailed description of the separated representation of $a(\bullet, \bullet)$ from (24) and gives the matrix structure of the problem. The separation of $a(\bullet, \bullet)$ into products of modes is given by

$$a(\boldsymbol{Y}X, \boldsymbol{Y}^*X^*) = \sum_{I=1}^{4} m_I(X, X^*)\, a_I(\boldsymbol{Y}, \boldsymbol{Y}^*). \tag{A.1}$$

Here, $\boldsymbol{Y}^*$ and X^* denotes either $\boldsymbol{Y}_N$ and X_N or $\delta\boldsymbol{Y}$ and δX, respectively. Moreover, $m_I(\bullet, \bullet)$ and $a_I(\bullet, \bullet)$ are bilinear forms on the separated domains defined according to

$$m_1(X, X^*) = \int_{I_x} X\, X^*\, dx, \qquad\qquad a_1(\boldsymbol{Y}, \boldsymbol{Y}^*) = \int_{\hat{\Omega}} \hat{\epsilon}[\boldsymbol{Y}] : \mathbf{E} : \hat{\epsilon}[\boldsymbol{Y}^*]\, d\hat{\Omega}, \tag{A.2a}$$

$$m_2(X, X^*) = \int_{I_x} \frac{dX}{dX}\, X^*\, dx, \qquad\qquad a_2(\boldsymbol{Y}, \boldsymbol{Y}^*) = \int_{\hat{\Omega}} \hat{\epsilon}[\boldsymbol{Y}] : \mathbf{E} : \epsilon_X[\boldsymbol{Y}^*]\, d\hat{\Omega}, \tag{A.2b}$$

$$m_3(X, X^*) = \int_{I_x} X\, \frac{dX^*}{dx}\, dx, \qquad\qquad a_3(\boldsymbol{Y}, \boldsymbol{Y}^*) = \int_{\hat{\Omega}} \epsilon_X[\boldsymbol{Y}] : \mathbf{E} : \hat{\epsilon}[\boldsymbol{Y}^*]\, d\hat{\Omega}, \tag{A.2c}$$

$$m_4(X, X^*) = \int_{I_x} \frac{dX}{dx}\, \frac{dX^*}{dx}\, dx, \qquad\qquad a_4(\boldsymbol{Y}, \boldsymbol{Y}^*) = \int_{\hat{\Omega}} \epsilon_X[\boldsymbol{Y}] : \mathbf{E} : \epsilon_X[\boldsymbol{Y}^*]\, d\hat{\Omega}. \tag{A.2d}$$

where the separated representation of the strain was defined in (25). It allows for computing the integrals separately. However, this separation is not possible for ϵ^p, which is why $b(\epsilon^p, \boldsymbol{Y}^*X^*)$ is expressed as

$$b(\epsilon^p, \boldsymbol{Y}^*X^*) = \int_{I_x} \int_{\hat{\Gamma}_N} \left(X^*\hat{\epsilon}[\boldsymbol{Y}^*] + \frac{dX^*}{dx}\epsilon_X[\boldsymbol{Y}^*] \right) : \mathbf{E} : \epsilon^p\, d\hat{\Omega}\, dx. \tag{A.3}$$

Finally, (24) can be explicitly written as finding $X_N \in \mathbb{X}$ and $\boldsymbol{Y}_N \in \mathbb{Y}$, with the function spaces defined in (22), such that

$$\sum_{I=1}^{4} m_I(X_N, X_N) a_I(\boldsymbol{Y}_N, \delta\boldsymbol{Y}) = b(\epsilon^p, \delta\boldsymbol{Y}X_N) - \sum_{n=1}^{N-1}\sum_{I=1}^{4} m_I(X_n, X_N) a_I(\boldsymbol{Y}_n, \delta\boldsymbol{Y}) \quad \forall \delta\boldsymbol{Y} \in \mathbb{Y}, \tag{A.4a}$$

$$\sum_{I=1}^{4} m_I(X_N, \delta X) a_I(\boldsymbol{Y}_N, \boldsymbol{Y}_N) = b(\epsilon^p, \boldsymbol{Y}_N \delta X) - \sum_{n=1}^{N-1}\sum_{I=1}^{4} m_I(X_n, \delta X) a_I(\boldsymbol{Y}_n, \boldsymbol{Y}_N) \quad \forall \delta X \in \mathbb{X}. \tag{A.4b}$$

In (A.4a) and (A.4b), we observe descriptions of the 2D and 1D problems, respectively.

To solve the modes in the enrichment step N, a fixed-point alternating algorithm is adopted to find $\boldsymbol{Y}_N(y)$ and $X_N(x)$. This procedure is explained in more detail in [36]. The fixed-point iterations continue until the weighted difference Δ between two iteration steps is smaller than a tolerance ϵ_{PGD}, i.e., until

$$\Delta := \sqrt{|\Delta\alpha_N|^2 + \|\Delta\hat{Y}_N\|_{\mathrm{Y}}^2 + \|\Delta\hat{X}_N\|_{\mathrm{X}}^2} < \epsilon_{\mathrm{PGD}}, \tag{A.5a}$$

$$\alpha_N = \|Y_N\|_{\mathrm{Y}} \, \|X_N\|_{\mathrm{X}}, \tag{A.5b}$$

$$\hat{Y}_N = \frac{Y_N}{\|Y_N\|_{\mathrm{Y}}}, \quad \|Y\|_{\mathrm{Y}} := \sqrt[4]{\sum_{I=1}^{4}[a_I(Y,Y)]^2}, \tag{A.5c}$$

$$\hat{X}_N = \frac{X_N}{\|X_N\|_{\mathrm{X}}}, \quad \|X\|_{\mathrm{X}} := \sqrt[4]{\sum_{I=1}^{4}[m_I(X,X)]^2}. \tag{A.5d}$$

Here, α_N and $\hat{Y}_N$, $\hat{X}_N$ are the amplitude and the normalized mode shapes, respectively.

To numerically solve the PGD approximation of the displacement field, linear finite elements are used. The FE-subspaces are defined as $\mathbb{Y}_h \subset \mathbb{Y}$ and $\mathbb{X}_h \subset \mathbb{X}$. The nodal approximations for Y^* and X^*, along with the strains, are represented as

$$Y^*(y) \approx \sum_{i=1}^{NDOF_y} N_i^{(\mathrm{y})}(y)(\underline{Y}^*)_i \in \mathbb{Y}_h, \tag{A.6a}$$

$$X^*(x) \approx \sum_{i=1}^{NDOF_x} N_i^{(\mathrm{x})}(x)(\underline{X}^*)_i \in \mathbb{X}_h, \quad \frac{dX^*(x)}{dx} \approx \sum_{i=1}^{NDOF_x} B_i(x)(\underline{X}^*)_i \in \mathbb{X}_h, \tag{A.6b}$$

$$\hat{e}[Y^*(y)] \approx \sum_{i=1}^{NDOF_y} \hat{e}[N_i^{(\mathrm{y})}(y)](\underline{Y}^*)_i = \sum_{i=1}^{NDOF_y} B_i^{(\Omega)}(y)(\underline{Y}^*)_i, \tag{A.6c}$$

$$\epsilon_{\mathrm{X}}[Y^*(y)] \approx \sum_{i=1}^{NDOF_y} \epsilon_{\mathrm{X}}[N_i^{(\mathrm{y})}(y)](\underline{Y}^*)_i = \sum_{i=1}^{NDOF_y} B_i^{(\mathrm{x})}(y)(\underline{Y}^*)_i. \tag{A.6d}$$

Here, $N^{(\mathrm{y})}(y)$ and $N^{(\mathrm{x})}(x)$ are the FE shape functions while $\underline{Y}^*$ and $\underline{X}^*$ are vectors that contain nodal values in the FE mesh of the in- and out-of-plane parameters, respectively. The summation extends to each parameter's Number of Degrees Of Freedom (NDOF).

Using the FE-approximations on (24) leads to the discrete representation of the problem

$$\tilde{a}(\underline{Y}_N \, \underline{X}_N, \delta\underline{Y} \, \underline{X}_N) = [\underline{X}_N]^{\mathrm{T}}\underline{G} \, \delta\underline{Y} - \sum_{n=1}^{N-1} \tilde{a}(\underline{Y}_n \, \underline{X}_n, \delta\underline{Y} \, \underline{X}_N), \tag{A.7a}$$

$$\tilde{a}(\underline{Y}_N \, \underline{X}_N, \underline{Y}_N \, \delta\underline{X}) = [\delta\underline{X}]^{\mathrm{T}}\underline{G} \, \underline{Y}_N - \sum_{n=1}^{N-1} \tilde{a}(\underline{Y}_n \, \underline{X}_n, \underline{Y}_N \, \delta\underline{X}), \tag{A.7b}$$

where the FE-discretized bilinear form $\tilde{a}(\bullet, \bullet)$ is defined from (A.1) and (A.2) as

$$\tilde{a}(\underline{Y} \, \underline{X}, \underline{Y}^* \underline{X}^*) = \left([\underline{X}^*]^{\mathrm{T}}\underline{M}_\Omega \, \underline{X}\right)\left([\underline{Y}^*]^{\mathrm{T}}\underline{K}_\Omega \, \underline{Y}\right) + \left([\underline{X}^*]^{\mathrm{T}}\underline{M}_{\Omega\mathrm{X}} \, \underline{X}\right)\left([\underline{Y}^*]^{\mathrm{T}}\underline{K}_{\Omega\mathrm{X}} \, \underline{Y}\right)$$
$$+ \left([\underline{X}]^{\mathrm{T}}\underline{M}_{\mathrm{X}\Omega} \, \underline{X}^*\right)\left([\underline{Y}^*]^{\mathrm{T}}\underline{K}_{\mathrm{X}\Omega} \, \underline{Y}\right) + \left([\underline{X}]^{\mathrm{T}}\underline{M}_{\mathrm{X}} \, \underline{X}^*\right)\left([\underline{Y}^*]^{\mathrm{T}}\underline{K}_{\mathrm{X}} \, \underline{Y}\right). \tag{A.8}$$

The global stiffness matrices $\underline{K}$, mass matrices $\underline{M}$ are given by

$$(\underline{K}_\Omega)_{kl} = \int_{\hat{\Omega}} B_k^{(\Omega)}(y) : \mathsf{E} : B_l^{(\Omega)}(y) \; \mathrm{d}\hat{\Omega}, \qquad\qquad (\underline{M}_\Omega)_{kl} = \int_{I_\mathrm{x}} N_k^{(\mathrm{x})}(x) \cdot N_l^{(\mathrm{x})}(x) \; \mathrm{d}x, \tag{A.9a}$$

$$(\underline{K}_{\Omega\mathrm{X}})_{kl} = \int_{\hat{\Omega}} B_k^{(\Omega)}(y) : \mathsf{E} : B_l^{(\mathrm{x})}(y) \; \mathrm{d}\hat{\Omega}, \qquad\qquad (\underline{M}_{\Omega\mathrm{X}})_{kl} = \int_{I_\mathrm{x}} B_k(x) \cdot N_l^{(\mathrm{x})}(x) \; \mathrm{d}x, \tag{A.9b}$$

$$(\underline{K}_{\mathrm{X}\Omega})_{kl} = (\underline{K}_{\Omega\mathrm{X}})_{lk}, \qquad\qquad (\underline{M}_{\mathrm{X}\Omega})_{kl} = (\underline{M}_{\Omega\mathrm{X}})_{lk}, \tag{A.9c}$$

$$(\underline{K}_{\mathrm{X}})_{kl} = \int_{\hat{\Omega}} B_k^{(\mathrm{x})}(y) : \mathsf{E} : B_l^{(\mathrm{x})}(y) \; \mathrm{d}\hat{\Omega}, \qquad\qquad (\underline{M}_{\mathrm{X}})_{kl} = \int_{I_\mathrm{x}} B_k(x) \cdot B_l(x) \; \mathrm{d}x. \tag{A.9d}$$

These matrices are precomputed, while the external force matrix $\underline{G}$

$$(\underline{G})_{kl} = \int_{I_\mathrm{x}} \int_{\hat{\Omega}} \left(B_k^{(\Omega)}(y) : \mathsf{E} : (\epsilon^{\mathrm{p}}[y_k])_l N_l^{(\mathrm{x})}(x) + B_k^{(\mathrm{x})}(y) : \mathsf{E} : (\epsilon^{\mathrm{p}}[y_k])_l B_l(x) \right) \; \mathrm{d}\hat{\Omega} \; \mathrm{d}x, \tag{A.10}$$

is computed in each fixed-point iteration, see Section 4.4, after ϵ^{p} has been determined. These matrices facilitate the determination of mode shapes $\underline{Y}$ and $\underline{X}$ for solving u^{p} as

$$u^{\mathrm{p}} \approx u_N^{\mathrm{PGD}} = \sum_{n=1}^{N} \underline{Y}_n \, \underline{X}_n. \tag{A.11}$$

Appendix B. Newton iteration plasticity integration

This Section describes how to solve the evolution equations expressed via the BE-method in (28) using Newton iterations. The solution applies to a specific streamline k in the cross-section, and between two integration points out-of-plane, $[x_{n-1}, x_n] \in I_\mathrm{x}$.

The evolution equations can be expressed as the residual vector $\underline{R}$ and the vector of unknowns $\underline{X}$, which includes stress σ, back-stress α, and the plastic multiplier increment μ. This is expressed as

$$\underline{R}(\underline{X}) = \underline{0} \text{ with } \underline{X} = \begin{bmatrix} \sigma \\ \alpha \\ \mu \end{bmatrix}, \quad \underline{R} = \begin{bmatrix} R_\sigma \\ R_\alpha \\ R_\mu \end{bmatrix}. \tag{B.12}$$

For each streamline y in the cross-section, the iterative procedure for solving $\underline{X}$ is based on the known quantities from the previous integration point, $^{n-1}\sigma(y)$ and $^{n-1}\alpha^i(y)$. The initial values for the plastic strain and back-stress are given as $^0\epsilon^p(y) = \epsilon_{in}^p(y)$ and $^0\alpha^i(y) = \alpha_{in}^i(y)$, respectively.

For each integration point x_n, the Newton iteration procedure is outlined as follows:

1. **Compute an initial elastic trial solution:** Compute the trial stress σ^{tr} from (28a) and set $\alpha^{tr,i} = {}^{n-1}\alpha^i$, which is carried over from the previous integration point x_{n-1}.
2. **Check for yielding:** Use the yield function Φ^{tr} (4) to determine whether the material has yielded based on the trial solution.

   - If no yielding has occurred ($\Phi^{tr} < 0$), retain the trial stress $\sigma = \sigma^{tr}$, set the plastic strain increment to zero $\Delta\epsilon^p = 0$, and maintain the back-stress from the previous integration point $^n\alpha^i = \alpha^{tr,i}$.
   - If yielding has occurred, proceed to the Newton iteration process.

3. **Newton iteration procedure:** If yielding is detected, the solution is updated iteratively until convergence:

   - Calculate the unbalanced residual vector $\underline{R}^{(j)}$ given the values $\underline{X}^{(j)}$ in iteration j.
   - Check for convergence, if the norm of the unbalanced stress $|\underline{R}^{(j)}|$ is below a predefined tolerance, terminate the iterations.
   - If convergence is not achieved, compute the Jacobian $\underline{J}^{(j)}$ and use it to calculate an improved solution:

     $$\underline{X}^{(j+1)} = \underline{X}^{(j)} - [\underline{J}^{(j)}]^{-1}\underline{R}^{(j)}, \quad j = j + 1.$$

   - Repeat this step until convergence is achieved.

4. **Move on to the next integration point:** Once the solution has converged at the current integration point, move to the next point and repeat steps 1–3 for all integration points until $n = N$.

This iterative procedure is repeated for each streamline y in the cross-section.

Data availability

No data was used for the research described in the article.

References

[1] R. Skrypnyk, J.C.O. Nielsen, M. Ekh, B.A. Pålsson, Metamodelling of wheel–rail normal contact in railway crossings with elasto-plastic material behaviour, Eng. Comput. 35 (1) (2019) 139–155, http://dx.doi.org/10.1007/s00366-018-0589-3, [Online]. Available: http://link.springer.com/10.1007/s00366-018-0589-3.

[2] R. Skrypnyk, M. Ekh, J.C.O. Nielsen, B.A. Pålsson, Prediction of plastic deformation and wear in railway crossings – Comparing the performance of two rail steel grades, Wear 428–429 (2019) 302–314, http://dx.doi.org/10.1016/j.wear.2019.03.019, [Online]. Available: https://www.sciencedirect.com/science/article/pii/S0043164818308081.

[3] R. Skrypnyk, B.A. Pålsson, J.C.O. Nielsen, M. Ekh, On the influence of crossing angle on long-term rail damage evolution in railway crossings, Int. J. Rail Transp. 9 (6) (2021) 503–519, http://dx.doi.org/10.1080/23248378.2020.1864794, [Online]. Available: https://doi.org/10.1080/23248378.2020.1864794.

[4] R. Skrypnyk, U. Ossberger, B.A. Pålsson, M. Ekh, J.C.O. Nielsen, Long-term rail profile damage in a railway crossing: Field measurements and numerical simulations, Wear 472–473 (2021) http://dx.doi.org/10.1016/j.wear.2020.203331, [Online]. Available: https://www.sciencedirect.com/science/article/pii/S004316482030079X.

[5] C. Ansin, B.A. Pålsson, M. Ekh, F. Larsson, R. Larsson, Simulation and field measurement of the long-term rail surface damage due to plasticity, wear and surface rolling contact fatigue cracks in a curve, in: 12th International Conference on Contact Mechanics and Wear of Rail/Wheel Systems, Melbourne, Australia, 2022, p. 11.

[6] Z. Zhou, W. Li, Z. Wen, S. Zhou, G. Tao, Three-dimensional elastic–plastic stress analysis of wheel–rail cyclic rolling contact using finite element method, Wear 542–543 (2024) 205277, http://dx.doi.org/10.1016/j.wear.2024.205277, [Online]. Available: https://www.sciencedirect.com/science/article/pii/S0043164824000425.

[7] C.L. Pun, Q. Kan, P.J. Mutton, G. Kang, W. Yan, An efficient computational approach to evaluate the ratcheting performance of rail steels under cyclic rolling contact in service, Int. J. Mech. Sci. 101–102 (2015) 214–226, http://dx.doi.org/10.1016/j.ijmecsci.2015.08.008, [Online]. Available: https://www.sciencedirect.com/science/article/pii/S0020740315002957.

[8] J. Zhao, H. Miao, Q. Kan, P. Fu, L. Ding, G. Kang, P. Wang, Numerical investigation on the rolling contact wear and fatigue of laser dispersed quenched U71Mn rail, Int. J. Fatigue 143 (2021) 106010, http://dx.doi.org/10.1016/j.ijfatigue.2020.106010, [Online]. Available: https://www.sciencedirect.com/science/article/pii/S0142112320305429.

[9] J.P. Srivastava, P.K. Sarkar, V.R.K. Meesala, V. Ranjan, Rolling contact fatigue life of rail for different slip conditions, Lat. Am. J. Solids Struct. 14 (2017) 2243–2264, http://dx.doi.org/10.1590/1679-78254161, [Online]. Available: https://www.scielo.br/j/lajss/a/NVGsfzvWKLmFxZChGn7SSgs/?lang=en.

[10] Z. Wen, X. Jin, Y. Jiang, Elastic-plastic finite element analysis of nonsteady state partial slip wheel-rail rolling contact, J. Tribol. 127 (4) (2005) 713–721, http://dx.doi.org/10.1115/1.2033898, [Online]. Available: https://doi.org/10.1115/1.2033898.

[11] K.D. Van, M.H. Maitournam, Steady-state flow in classical elastoplasticity: Applications to repeated rolling and sliding contact, J. Mech. Phys. Solids 41 (11) (1993) 1691–1710, http://dx.doi.org/10.1016/0022-5096(93)90027-D, [Online]. Available: https://www.sciencedirect.com/science/article/pii/002250969390027D.

[12] K.D. Van, M. Maitournam, B. Prasil, Elastoplastic analysis of repeated moving contact application to railways damage phenomena, Wear 196 (1–2) (1996) 77–81, http://dx.doi.org/10.1016/0043-1648(95)06864-3, [Online]. Available: https://linkinghub.elsevier.com/retrieve/pii/0043164895068643.

[13] K.D. Van, M.H. Maitournam, On some recent trends in modelling of contact fatigue and wear in rail, Wear 253 (1) (2002) 219–227, http://dx.doi.org/10.1016/S0043-1648(02)00104-7, [Online]. Available: https://www.sciencedirect.com/science/article/pii/S0043164802001047.

[14] W. Shen, D.J. Kirkner, Non-linear finite-element analysis to predict permanent deformations in pavement structures under moving loads, Int. J. Pavement Eng. 2 (3) (2001) 187–199, http://dx.doi.org/10.1080/10298430108901726, [Online]. Available: https://doi.org/10.1080/10298430108901726. Publisher: Taylor & Francis _eprint: https://doi.org/10.1080/10298430108901726.

[15] A. Anantheswar, I. Wollny, M. Kaliske, A dynamic ALE formulation for structures under moving loads, Comput. Mech. 73 (1) (2024) 139–157, http://dx.doi.org/10.1007/s00466-023-02360-5, [Online]. Available: https://doi.org/10.1007/s00466-023-02360-5.

[16] U. Nackenhorst, On the finite element analysis of steady state rolling contact, WIT Trans. Eng. Sci. 1 (1970) 53–60.

[17] S. Damme, U. Nackenhorst, A. Wetzel, B.W. Zastrau, On the numerical analysis of the wheel-rail system in rolling contact, in: K. Popp, W. Schiehlen (Eds.), System Dynamics and Long-Term Behaviour of Railway Vehicles, Track and Subgrade, Springer, Berlin, Heidelberg, 2003, pp. 155–174, http://dx.doi.org/10.1007/978-3-540-45476-2_10.

[18] U. Nackenhorst, The ALE-formulation of bodies in rolling contact: Theoretical foundations and finite element approach, Comput. Methods Appl. Mech. Engrg. 193 (39) (2004) 4299–4322, http://dx.doi.org/10.1016/j.cma.2004.01.033, [Online]. Available: https://www.sciencedirect.com/science/article/pii/S0045782504002233.

[19] C. Chang, C. Wang, B. Chen, L. Li, A study of a numerical analysis method for the wheel-rail wear of a heavy-haul train, Proc. Inst. Mech. Eng. Part F: J. Rail Rapid Transit. 224 (5) (2010) 473–482, http://dx.doi.org/10.1243/09544097JRRT341, [Online]. Available: https://doi.org/10.1243/09544097JRRT341.

[20] A. Draganis, F. Larsson, A. Ekberg, Numerical evaluation of the transient response due to non-smooth rolling contact using an arbitrary Lagrangian–Eulerian formulation, Proc. Inst. Mech. Eng. Part J: J. Eng. Tribol. 226 (1) (2012) 36–45, http://dx.doi.org/10.1177/1350650111422015, [Online]. Available: https://doi.org/10.1177/1350650111422015.

[21] I. Wollny, M. Kaliske, Numerical simulation of pavement structures with inelastic material behaviour under rolling tyres based on an arbitrary Lagrangian Eulerian (ALE) formulation, Road Mater. Pavement Des. 14 (1) (2013) 71–89, http://dx.doi.org/10.1080/14680629.2012.735800, [Online]. Available: https://doi.org/10.1080/14680629.2012.735800. Publisher: Taylor & Francis _eprint: https://doi.org/10.1080/14680629.2012.735800.

[22] I. Wollny, F. Hartung, M. Kaliske, Numerical modeling of inelastic structures at loading of steady state rolling, Comput. Mech. 57 (5) (2016) 867–886, http://dx.doi.org/10.1007/s00466-016-1266-2, [Online]. Available: https://doi.org/10.1007/s00466-016-1266-2.

[23] S. Hazar, W. Zaki, Z. Moumni, G. Anlas, Modeling of steady-state crack growth in shape memory alloys using a stationary method, Int. J. Plast. 67 (2015) 26–38, http://dx.doi.org/10.1016/j.ijplas.2014.08.018, [Online]. Available: https://www.sciencedirect.com/science/article/pii/S0749641914001946.

[24] A. Ammar, B. Mokdad, F. Chinesta, R. Keunings, A new family of solvers for some classes of multidimensional partial differential equations encountered in kinetic theory modeling of complex fluids, J. Non-Newton. Fluid Mech. 139 (3) (2006) 153–176, http://dx.doi.org/10.1016/j.jnnfm.2006.07.007, [Online]. Available: https://www.sciencedirect.com/science/article/pii/S0377025706001662.

[25] A. Ammar, B. Mokdad, F. Chinesta, R. Keunings, A new family of solvers for some classes of multidimensional partial differential equations encountered in kinetic theory modelling of complex fluids: Part II: Transient simulation using space-time separated representations, J. Non-Newton. Fluid Mech. 144 (2) (2007) 98–121, http://dx.doi.org/10.1016/j.jnnfm.2007.03.009, [Online]. Available: https://www.sciencedirect.com/science/article/pii/S0377025707000821.

[26] F. Chinesta, R. Keunings, A. Leygue, The Proper Generalized Decomposition for Advanced Numerical Simulations, in: SpringerBriefs in Applied Sciences and Technology, Springer International Publishing, Cham, 2014, http://dx.doi.org/10.1007/978-3-319-02865-1, [Online]. Available: http://link.springer.com/10.1007/978-3-319-02865-1.

[27] A. Ammar, M. Normandin, F. Chinesta, Solving parametric complex fluids models in rheometric flows, J. Non-Newton. Fluid Mech. 165 (23) (2010) 1588–1601, http://dx.doi.org/10.1016/j.jnnfm.2010.08.006, [Online]. Available: https://www.sciencedirect.com/science/article/pii/S037702571000217X.

[28] E. Pruliere, F. Chinesta, A. Ammar, On the deterministic solution of multidimensional parametric models using the proper generalized decomposition, Math. Comput. Simulation 81 (4) (2010) 791–810, http://dx.doi.org/10.1016/j.matcom.2010.07.015, [Online]. Available: https://www.sciencedirect.com/science/article/pii/S0378475410002521.

[29] X. Zou, M. Conti, P. Díez, F. Auricchio, A nonintrusive proper generalized decomposition scheme with application in biomechanics, Internat. J. Numer. Methods Engrg. 113 (2) (2018) 230–251, http://dx.doi.org/10.1002/nme.5610, [Online]. Available: https://onlinelibrary.wiley.com/doi/abs/10.1002/nme.5610.

[30] E. Giner, B. Bognet, J.J. Ródenas, A. Leygue, F.J. Fuenmayor, F. Chinesta, The proper generalized decomposition (PGD) as a numerical procedure to solve 3D cracked plates in linear elastic fracture mechanics, Int. J. Solids Struct. 50 (10) (2013) 1710–1720, http://dx.doi.org/10.1016/j.ijsolstr.2013.01.039, [Online]. Available: https://www.sciencedirect.com/science/article/pii/S0020768313000541.

[31] D. González, A. Ammar, F. Chinesta, E. Cueto, Recent advances on the use of separated representations, Internat. J. Numer. Methods Engrg. 81 (5) (2010) 637–659, http://dx.doi.org/10.1002/nme.2710, [Online]. Available: https://onlinelibrary.wiley.com/doi/abs/10.1002/nme.2710.

[32] E. Cueto, D. González, I. Alfaro, Proper Generalized Decompositions, SpringerBriefs in Applied Sciences and Technology, Springer International Publishing, Cham, 2016, http://dx.doi.org/10.1007/978-3-319-29994-5, [Online]. Available: http://link.springer.com/10.1007/978-3-319-29994-5.

[33] L. Chamoin, F. Pled, P.-E. Allier, P. Ladevèze, A posteriori error estimation and adaptive strategy for PGD model reduction applied to parametrized linear parabolic problems, Comput. Methods Appl. Mech. Engrg. 327 (2017) 118–146, http://dx.doi.org/10.1016/j.cma.2017.08.047, [Online]. Available: https://www.sciencedirect.com/science/article/pii/S0045782517306357.

[34] A. Ammar, F. Chinesta, P. Diez, A. Huerta, An error estimator for separated representations of highly multidimensional models, Comput. Methods Appl. Mech. Engrg. 199 (25) (2010) 1872–1880, http://dx.doi.org/10.1016/j.cma.2010.02.012, [Online]. Available: https://www.sciencedirect.com/science/article/pii/S0045782510000708.

[35] F. Chinesta, A. Ammar, E. Cueto, Recent advances and new challenges in the use of the proper generalized decomposition for solving multidimensional models, Arch. Comput. Methods Eng. 17 (4) (2010) 327–350, http://dx.doi.org/10.1007/s11831-010-9049-y, [Online]. Available: https://doi.org/10.1007/s11831-010-9049-y.

[36] C. Ansin, F. Larsson, R. Larsson, Fast simulation of 3D elastic response for wheel–rail contact loading using proper generalized decomposition, 116466, Comput. Methods Appl. Mech. Engrg. 417 (116466) (2023) 22, http://dx.doi.org/10.1016/j.cma.2023.116466, [Online]. Available: https://www.sciencedirect.com/science/article/pii/S004578252300590X.

[37] B. Bognet, F. Bordeu, F. Chinesta, A. Leygue, A. Poitou, Advanced simulation of models defined in plate geometries: 3D solutions with 2D computational complexity, Comput. Methods Appl. Mech. Engrg. 201–204 (2012) 1–12, http://dx.doi.org/10.1016/j.cma.2011.08.025, [Online]. Available: https://www.sciencedirect.com/science/article/pii/S0045782511002891.

[38] B. Bognet, A. Leygue, F. Chinesta, On the fully 3D simulations of thermoelastic models defined in plate and shell geometries, Eur. J. Comput. Mech. 21 (1–2) (2012) 40–51, http://dx.doi.org/10.1080/17797179.2012.702429, [Online]. Available: https://www.tandfonline.com/doi/full/10.1080/17797179.2012.702429.

[39] J. Ayasse, H. Chollet, Determination of the wheel rail contact patch in semi-Hertzian conditions, Veh. Syst. Dyn. 43 (3) (2005) 161–172, http://dx.doi.org/10.1080/00423110412331327193, [Online]. Available: https://doi.org/10.1080/00423110412331327193.

[40] X. Quost, M. Sebes, A. Eddhahak, J.-B. Ayasse, H. Chollet, P.-E. Gautier, F. Thouverez, Assessment of a semi-Hertzian method for determination of wheel–rail contact patch, Veh. Syst. Dyn. 44 (10) (2006) 789–814, http://dx.doi.org/10.1080/00423110600677948, [Online]. Available: https://doi.org/10.1080/00423110600677948.

[41] H. Hertz, On the contact of solid, elastic bodies, J. R. Angew. Math. 92 (1882) 156–171.

[42] N. Ohno, J.-D. Wang, Kinematic hardening rules with critical state of dynamic recovery, part I: formulation and basic features for ratchetting behavior, Int. J. Plast. 9 (3) (1993) 375–390, http://dx.doi.org/10.1016/0749-6419(93)90042-O, [Online]. Available: https://www.sciencedirect.com/science/article/pii/074964199390042O.

[43] R. Brommesson, M. Ekh, M. Hörnqvist, Correlation between crack length and load drop for low-cycle fatigue crack growth in Ti-6242, Int. J. Fatigue 81 (2015) 1–9, http://dx.doi.org/10.1016/j.ijfatigue.2015.07.006, [Online]. Available: https://www.sciencedirect.com/science/article/pii/S0142112315002157.

[44] J. Ahlström, B. Karlsson, Fatigue behaviour of rail steel—a comparison between strain and stress controlled loading, Wear 258 (7) (2005) 1187–1193, http://dx.doi.org/10.1016/j.wear.2004.03.030, [Online]. Available: https://www.sciencedirect.com/science/article/pii/S0043164804002856.

[45] C3SE-Chalmers, Vera - C3SE, 2024, [Online]. Available: https://www.c3se.chalmers.se/about/Vera/.